Published in final edited form as:

Nat Neurosci. 2022 June ; 25(6): 702–713. doi:10.1038/s41593-022-01057-x.

Candelabrum cells are ubiquitous cerebellar cortex interneurons with specialized circuit properties

Tomas Osorno[1,*], **Stephanie Rudolph**[1,4,*], **Tri Nguyen**[1], **Velina Kozareva**[2], **Naeem Nadaf**[2], **Aliya Norton**[1], **Evan Z. Macosko**[2], **Wei-Chung Allen Lee**[3], **Wade G. Regehr**[1,5]

[1]Department of Neurobiology, Harvard Medical School, 220 Longwood Ave, Boston MA 02115

[2]Broad Institute of Harvard and MIT, Stanley Center for Psychiatric Research, 450 Main St., Cambridge MA USA.

[3]F.M. Kirby Neurobiology Center, Boston Children's Hospital, Harvard Medical School, 220 Longwood Ave, Boston MA 02115.

[4]Current Address: Albert Einstein College of Medicine, New York, NY 10461.

Abstract

To understand how the cerebellar cortex transforms mossy fiber (MF) inputs into Purkinje cell (PC) outputs, it is vital to delineate the elements of this circuit. Candelabrum cells (CCs) are enigmatic interneurons of the cerebellar cortex that have been identified based on their morphology, but their electrophysiological properties, synaptic connections, and function remain unknown. Here, we clarify these properties using electrophysiology, snRNA sequencing, *in situ* hybridization, and serial electron microscopy in mice. We find that CCs are the most abundant PC layer interneuron. They are GABAergic, molecularly distinct, and present in all cerebellar lobules. Their high resistance renders CC firing highly sensitive to synaptic inputs. CCs are excited by MFs and granule cells, and strongly inhibited by PCs. CCs in turn primarily inhibit molecular layer interneurons, which leads to PC disinhibition. Thus, inputs, outputs and local signals converge onto CCs to allow them to assume a unique role in controlling cerebellar output.

Introduction

The cerebellum controls fine motor coordination, motor learning, eye movements, balance, and cognitive-affective functions, in addition to many behaviors that depend on prediction[1–4]. The cerebellar cortex is thought to contribute to these functions by

[5]**Correponding author** wade_regehr@hms.harvard.edu.

*Equal contribution

AUTHOR CONTRIBUTIONS

TO, SR and WGR designed experiments. TO and SR performed electrophysiology experiments. T.N. generated the automated segmentations in the serial EM dataset. N.N. performed smFISH experiments. TO analyzed electrophysiology, smFISH and serial EM data. AN analyzed serial EM data. V.K. and E.M. analyzed snRNAseq data. TO, SR and WGR wrote the paper with input from all authors.

COMPETING INTERESTS

The authors declare no competing interests.

transforming multimodal sensory and higher-order inputs from mossy fibers (MFs) into Purkinje cell (PC) outputs. Within the cerebellar cortex, few MFs excite many granule cells that in turn form weak synapses onto a moderate number of PCs. Inhibitory interneurons contribute to information processing at all stages. Golgi cells regulate granule cell excitability and MF integration in the input layer[5–7]. Molecular layer interneurons (MLIs) inhibit PCs to control the output of the cerebellar cortex[8, 9]. Although the simplicity of this circuit holds great promise for determining how circuit level computations contribute to behavior, the cerebellum contains additional elements that are neglected in current circuit models. It is particularly important to delineate these cell types for the cerebellar cortex, where only eight types of interneurons have been identified[10], compared to 50–60 types of inhibitory interneurons within the cerebral cortex[11–14].

The candelabrum cell (CC) of the cerebellar cortex is a particularly intriguing type of neuron. CCs were identified in 1994 based on their distinctive light-level morphology[15]. CCs have a small cell body near the Purkinje cell layer (PCL), dendrites that extend to the surface of the molecular layer, and beaded axons that make numerous local synapses within the molecular layer. Thus far, due to the lack of electrophysiological recordings and specific molecular markers, nothing beyond anatomical features is known about CCs. In our recent single nucleus RNA sequencing (snRNAseq) study we identified three types of molecularly distinct inhibitory interneurons in the cerebellar cortex that are neither MLIs nor Golgi cells[10]. These findings may provide insight into the molecular properties of CCs, but a link between these molecularly defined populations and CCs has not been established.

Here, we use a combination of mouse genetics, snRNA sequencing, *in situ* hybridization, electrophysiology and serial electron microscopy (EM) to characterize CCs. We identified a transgenic mouse line in which CCs are fluorescently labelled, allowing us to record from them. We found that CCs are highly sensitive to small depolarizations and present in all cerebellar lobules. Electrophysiology and serial EM reconstructions establish that MFs and granule cells are the main excitatory inputs to CCs, PCs the main inhibitory inputs, and MLIs are the primary targets of CCs. Prolonged CC firing disinhibits PCs. CCs are thus part of an inhibitory loop between MLIs and PCs. The integration of MF, PC and granule cell inputs suggests that their function is distinct from that of MLIs and Golgi cells. Therefore, CCs are an important interneuron that need to be incorporated into circuit models to gain a full understanding of cerebellar processing.

RESULTS

Morphology and electrophysiology of Candelabrum cells

Recording from CCs is vital to clarifying their function. The CCs' location in the PCL, in the proximity of more abundant granule cells, MLIs and Bergmann glia that are similar in cell body size, has complicated previous attempts. It is also difficult to identify CCs using mice that express GFP in GABAergic glutamate-decarboxylase-67 positive neurons because CCs are typically obscured by much brighter PCs. Fortunately, we found that in oxytocin receptor Cre mice crossed to a *flox* tdTomato line (Oxtr-Cre × Ai14), small PCL interneurons (PLIs) consistent with CC anatomy are labelled (Fig. 1A). MFs and a small

number of MLIs and PCs were also labelled, but they were readily distinguished from PLIs based on their position, shape, and size.

We filled tdTomato+ PLIs with Alexa-594 during whole-cell recordings in brain slices and used 2-photon imaging to determine their morphology. All labelled cells exhibited the characteristic morphology of CCs, with small cell bodies (~10 μm in diameter) located in the PCL, one or two primary dendrites that ascend to the pia and branch within the upper molecular layer, several secondary dendrites that extend to the upper part of the granular layer, and a beaded axon emanating from near the soma that branches and extends in the molecular layer (Fig. 1B, Extended Data Fig. 1). Dendrites were confined to a parasagittal plane, but the axon and its associated boutons extended beyond the plane in the z direction (Extended Data Fig. 1B–D). The stereotyped morphology of these neurons is in concordance with the original description of CCs[15], and we conclude that we can consistently record from CCs in Oxtr-Cre × Ai14 mice.

In cell-attached recordings and whole-cell current clamp recordings, CCs were mostly silent, although some fired spontaneously, with varying frequencies and regularity (Fig. 1C, G). In voltage-clamp recordings, high-frequency spontaneous IPSCs were observed that were blocked by the $GABA_A$-receptor antagonist gabazine (10 μM; Fig. 1D, G). Input-output curves show that CCs are extremely sensitive to current injection (Fig. 1E, F), in contrast with the two types of MLIs, MLI1 and MLI2, that are much less sensitive (Fig. 1F)[10]. A summary of the basic electrophysiological properties of CCs (Fig. 1G) suggests that their most distinctive characteristics are high excitability and high frequencies of sIPSCs.

Molecular insights into cerebellar cortex interneurons

Our previous molecular characterization of cerebellar cell types has the potential to provide insight into the molecular identity of CCs. We used snRNAseq data to molecularly characterize neurons of the adult cerebellar cortex and identified eight clusters of inhibitory interneurons[10]. In addition to MLIs (that can be subdivided into MLI1_1, MLI1_2, and MLI2), and Golgi cells (Golgi1 and Golgi2), we identified three types of inhibitory interneurons that we referred to as PLIs: PLI1, PLI2, and PLI3 (Fig. 2A). However, whether these molecularly defined cell types are anatomically and electrophysiologically defined cerebellar interneurons is unclear.

A summary of the expression of key genes showed that it is not always possible to delineate a cell type with a single gene[10, 16]. Rather, a combination of genes is required to demarcate distinct interneuron types, including PLI1s (Fig. 2B, C). The expression of *Htr2a* that encodes the 5-HT2A receptor, and *Slc6a5* that encodes the glycine transporter, by PLI3 suggests that this cell type corresponds to Lugaro cells, that are glycinergic and excited by serotonin[17]. Lugaro cells are GABAergic/glycinergic PLIs with a distinctive fusiform soma that are inhibited by PCs, and that locally inhibit Golgi cells and MLIs, and send long-range axons to unknown targets[17–24]. Lugaro cells and CCs have very different morphologies. PLI2s also express *Slc6a5*, which suggests that they correspond to globular cells (GLCs) that are glycinergic, located near or below the PCL, and inhibited by PCs[25, 26]. Globular cells and CCs also have very different morphologies[15, 25, 26]. This suggests that CCs might correspond to the remaining cell type, PLI1.

We next applied a method we developed previously[10] to characterize the relative discreteness versus continuity across the clustered populations. Briefly, we fit logistic curves to the expression of differentially expressed genes along the dominant pseudotime expression trajectory constructed across different pairs of interneuron populations. We then determined the maximum slope value of the fit, *m*, for 150 highly variable genes (Fig. 2D). High values of *m* indicate sharp transitions and suggest discrete cell types, whereas low values indicate smooth transitions and gradations in cell class. Cumulative distribution plots of *m* for different combinations of PLIs allowed us to assess the degree of similarity of different types of PLIs. PLI1 and PLI2 were most similar to each other because the *m* values tended to be small, whereas PLI1 and PLI3, and PLI2 and PLI3 are highly distinct, because the *m* values are large (Fig. 2D). The relationships between different types of PLIs is similar to the relationships we described previously for MLIs (Fig. 2E)[10], which can be subdivided into two distinct cell populations (MLI1 and MLI2, with MLI1 further subdivided into MLI1_1 and MLI1_2). The latter are much more similar to each other than they are to MLI2, just as PLI1 and PLI2 are much more similar to each other than they are to PLI3. MLI1_1 and MLI1_2 correspond to basket cells and stellate cells, respectively, which have distinctive morphologies, synapse distribution, and locations in the molecular layer. However, there are some intermediate MLIs that share properties of MLI1_1 and MLI1_2. Similarly, it is expected that while most PLI1 and PLI2 neurons have distinct properties, some cells share features of PLI1 and PLI2.

The expression of most genes varied gradually with pseudotime and were not very useful for discriminating between PLI1 and PLI2. However, *Slc6a5* expression as a function of pseudotime was approximated with a logistic fit with a maximum slope, *m*, of 3.03 (Fig. 2F). *Slc6a5* was detected in 48% (341/735) of PLI2s, but only 2% of PLI1s (28/1177 cells) (Fig. 2G). Despite the relative molecular similarity between PLI1 and PLI2 and occasional expression of *Slc6a5* in PLI1s, *Slc6a5* provides a promising means for discriminating between PLI1s and PLI2s.

Candelabrum cells are widespread in the cerebellar cortex

We used single molecule FISH (smFISH) in sagittal sections of adult cerebellar vermis to determine whether PLI1s correspond to CCs (Fig. 3). We combined probes for *Nxph1*, *Slc6a5* and *Aldh1a3* to label different PLI subpopulations. We then quantified the fluorescence for each labelled cell within the slice and determined its position (Fig. 3A–E, Extended Data Fig. 2). Fluorescence images of individual cells (Fig. 3A), and average images and line profiles (Fig. 3B) are shown for the 3 labels and for each cell type. The combined expression of these 3 markers allowed us to identify five populations of cells: PLI1s (*Nxph1*+, *Aldh1a3*+, *Slc6a5*−), PLI2s (*Nxph1*+, *Aldh1a3*+, *Slc6a5*+), Golgi1 cells (*Nxph1*−, *Aldh1a3*−, *Slc6a5*+), a mixed population that contains Golgi2 cells and PLI3s (*Nxph1*+, *Aldh1a3*−, *Slc6a5*+), and MLI2s (*Nxph1*+, *Aldh1a3*−, *Slc6a5*−).

We also determined the spatial distributions of the different cell types (Fig. 3C), quantified their numbers in different lobules (Fig. 3D), and determined their locations relative to the PCL (Fig. 3E), and there were no obvious sex-dependent differences (Extended Data Fig. 3). PLI1s were located in all lobules of the vermis, although their density was lower in

lobules VII, VIII, IX (Fig. 3C, 3D, Extended Data Fig. 3, *light blue*). PLI1s were clustered around the PCL, with a fraction of PLI1s extending into the lower third of the molecular layer (Fig. 3E, *light blue*). PLI1s were remarkably abundant, with the ratio of the number of given cell type to the number of PLI1s being: 0.70 PLI2, 1.22 Golgi1, 0.61 for combined Golgi2 and PLI3s, and 4.96 for MLI2. These ratios are consistent with estimates based on snRNAseq data, where the ratios were 0.62 (735/1177) for PLI2s and 0.45 (531/1177) for PLI3s (Extended Data Fig. 4). Thus, there are approximately the same number of PLI interneurons as Golgi cells, and CCs are the most abundant PLI interneuron.

In Oxtr-Cre × Ai14 mice, many small neurons of the PCL were labelled with tdTomato along with a small number of MLIs and PCs (Extended Data Fig. 5). The labeled MLIs and PCs were readily distinguished from small PLIs based on their position, shape, and size. We used two probes to characterize tdTomato+ neurons in Oxtr-Cre × Ai14 mice and used one fluorescence channel for tdTomato (Fig. 3F–J). Line profiles for tdTomato+ PLIs (Fig. 3G) show *Aldh1a3* labelling that is similar to that of PLI1s (Fig. 3B), and very low levels of *Slc6a5* (Fig. 3G), in contrast to the lack of *Slc6a5* expression used to identify PLI1s (Fig. 3B). This suggests that our *Slc6a5*− criteria excluded the rare *Slc6a5*+ PLI1s (Fig. 2FG), and that the PLI1 population identified in Fig.3A–E is a slight underestimate of the number of CCs. The distribution of tdTomato+ PLIs (Fig. 3I) is similar to that of PLI1s (Fig. 3D) with the exception of lobule X. This is likely because background tdTomato expression is prominent in lobule X, making it difficult to unambiguously identify tdTomato+ labelled PLIs in this region. Differences in the layer distributions of tdTomato+ cells in the lower molecular layer (Fig. 3J) compared to PLI1s (Fig. 3E), suggests that PLI1s in the lower molecular layer are not labelled in Oxtr-Cre × Ai14 mice. In summary, the combination of the tdTomato+ labelling of PLIs in Oxtr-Cre × Ai14 mice, fluorescent labelling and 2P imaging of these cells (Fig. 1), and *in situ* labelling of 3 genes identified by single cell characterization, establishes that tdTomato+ PLIs are CCs that correspond to PLI1s.

Excitatory synapses onto Candelabrum cells

The axons of granule cells, the parallel fibers, excite MLI, Golgi cell and PCs dendrites in the molecular layer. We tested whether granule cells also excite CCs. We stimulated parallel fibers and recorded synaptic currents in voltage clamp while blocking inhibition (Fig. 4A). We measured EPSCs from CCs at −65 mV and at +40 mV (Fig. 4B). A fast component was blocked by the AMPA receptor (AMPAR) antagonist NBQX, and the remaining slow component present at +40 mV was blocked by the NMDAR antagonist CPP. The presence of a prominent NMDA component is consistent with the expression of *Grin1* and *Grin2b* in CCs[10]. We also assessed the paired-pulse plasticity of the AMPA component of this synapse and found that closely-spaced stimulus pairs evoked facilitating responses typical of granule cell synapses onto other targets (Fig. 4C).

MFs form synapses mainly in the granule cell layer where they contact granule cells, Golgi cells and unipolar brush cells (UBCs), but they do not excite MLIs and PCs whose dendrites are restricted to the molecular layer. Although most CC dendrites are located within the molecular layer, their basal dendrites often extend into the upper granular layer (Fig. 1B, Extended Data Fig. 1). This raised the possibility that MFs might synapse onto

CCs. We tested this by stimulating MF axons in the white matter while blocking inhibition. Stimulation evoked short-latency NBQX-sensitive excitatory currents. Stimulation at the threshold for MF activation stochastically evoked successes and failures (Fig. 4D), and slight increases in stimulus intensity eliminated failures. This indicates that this is a single, all-or-none input. To determine whether inputs to CCs were monosynaptic, we compared the latency of white matter stimulation-evoked excitatory inputs onto both CCs and MLIs. The median latency for CCs was 1.45 ms compared to 4.52 ms for MLIs (Extended Data Fig. 6). This is consistent with a monosynaptic short-latency MF to CC connection, and long-latency disynaptic excitation of MLIs (MF→granule cell→MLI). Short-term plasticity of MF synapses ranged from slight paired-pulse depression to robust facilitation (Fig. 4E), similar to the highly variable paired-pulse plasticity of MF to granule and Golgi cell synapses[27, 28]

Lastly, we assessed whether climbing fibers excite CCs. Climbing fibers form powerful excitatory synapses onto PCs, and they also excite MLIs and Golgi cells as a result of glutamate spillover, even though they do not directly synapse onto these cells[29–32]. These spillover currents are quite small, slow, depress strongly, and are greatly enhanced by blocking glutamate uptake. We observed synaptic inputs to CCs with similar properties, although they were extremely small (10–20 pA, Extended Data Fig. 7) and rare (observed in 3 of 25 cells with a mean of 23 stimulus locations tested per cell). This suggests that climbing fibers can influence CC firing, but to a lesser extent than in MLIs and Golgi cells.

We also assessed connectivity by reconstructing CCs and their inputs in a serial EM volume of adult lobule V cerebellar cortex (Methods, Nguyen et al., 2021). CCs were identified in reconstructions based on their similarity to their distinctive light level morphologies (Fig. 1, Extended Data Fig. 1). We reconstructed all PLIs in the volume and identified CCs based on their characteristic morphological features: soma size, location and shape, primary dendrite branching in the molecular layer, proximal dendrites extending into the upper granule cell layer, and beaded axons in the molecular layer (Fig. 4F, Extended Data Fig. 8- *light blue*). We also reconstructed granule cell axons and MFs based on their characteristic morphology. (Fig. 4F, Extended Data Fig. 8AB - *MF:red, granule cell, GrC:gold*). Each granule cell sends an axon from the granular layer to the molecular layer where it bifurcates and extends in both directions and forms parallel fibers that intersect PC dendrites. We found that parallel fibers synapsed onto CC dendrites throughout the entire length of the primary dendrites (Fig. 4F, Extended Data Fig. 8AB). Ascending granule cell axons also synapsed onto CCs (Extended Data Fig. 8CD). MFs synapsed onto proximal basal dendrites. MF-CC synapses were of two different types. In some cases, a CC dendrite extended into a MF glomerulus and contacted a large MF bouton (Fig. 4F-*inset b*, Extended Data Fig. 8A, B-*inset b*), but in other cases a small MF branch contacted CC dendrites (Fig. 4F-**inset** a, Extended Data Fig. 8A-*inset a*). These reconstructions confirmed that CCs receive synaptic inputs from granule cells and MFs.

Inhibition of candelabrum cells

PCs are spontaneously active at high frequencies, and their collaterals form synapses near the PC layer[33]. We used PC-to-CC paired recordings to assess whether PCs inhibit CCs

and provide the high-frequency spontaneous IPSCs we observe in CCs. We recorded spontaneous PC firing in the loose patch configuration, and measured IPSCs in CCs in voltage clamp (Fig. 5A). Spike-triggered alignment of CC recordings revealed a short-latency outward current that was blocked by a $GABA_AR$ antagonist, consistent with direct PC-CC inhibition (Fig. 5B). PC-CC connections were short latency, had a wide range of average sizes, and accounted for a large fraction of the total spontaneous inhibition in CCs (Fig 5D).

We also assessed connectivity using serial EM reconstructions. A PC (Fig. 5E, *purple*) and a CC (Fig. 5E, light blue) are shown. We found that PC axon collaterals directly contact CC dendrites and somata, and that the same PC forms multiple synapses with a single CC (Fig. 5E, Extended Data Fig. 9AB), confirming that PCs directly synapse onto CCs. PC-CC connections were easy to identify, but MLI-CC connections were difficult to find. Nonetheless, we observed MLI to CC connections (Fig. 5A, Fig. 5C). Compared to PC-CC connections, MLI-CC connections show strong trends to being rarer, weaker, having a lower success probability and accounting for a lower fraction of the total inhibitory events observed in a CC (Fig. 5D), although the differences are not significant. EM reconstructions confirmed the presence of MLI to CC connections (Extended Data Fig. 9CD).

Candelabrum cells widely inhibit MLIs

The axons of CCs are in the PCL and molecular layer; therefore, their synaptic targets must be cells that have somata or dendrites in the molecular layer. We recorded spiking from CCs in loose patch or current clamp mode, and simultaneously recorded synaptic currents from either MLIs or PCs in voltage clamp (Fig. 6A, E). Although we expect CCs to release GABA as a primary transmitter, we did not exclude the possibility of other neurotransmitters; therefore, we omitted synaptic blockers from the bath solution and recorded postsynaptic currents at intermediate voltages between E_{Cl}- and the reversal potential of EPSCs (0 mV), as shown for a CC-MLI paired recording (Fig. 6B). IPSCs were blocked by bath application of SR-95531 (Fig. 6B, *red trace*). The amplitude histogram is shown for an example pair (Fig. 6C). We found that 10% (5/49) of CC-MLI pairs were connected, and the properties of these synapses are summarized in Fig. 6D. Similar experiments were performed to assess CC to PC connections, and we only observed a single connected pair (n= 1/83 pairs, 1%) (Fig. 6F). It is likely that we underestimate the fraction of cells inhibited by CCs because slicing can sever all or part of the CC axon.

We then identified CC synaptic boutons and their targets in EM reconstructions. We found that most CC synapses are made onto MLIs (92% of synapses), but CCs also synapse onto Golgi cells (4.8%), other cells (2.7% PLIs and unidentified cell types), and there was a single synapse onto a PC (Fig. 6G). These findings are in qualitative agreement with our electrophysiological studies that found CCs were more likely to inhibit MLIs than PCs. We found that a single CC can inhibit a great many nearby MLIs (Fig. 6I-*MLI grey, CC-light blue*) with a variable number of synapses per target ranging from 1 to >10 (Fig. 6H). Example high resolution views are shown for a target MLI (Fig. 6I- *orange, insets a, b*). Whereas CCs contact a large fraction of nearby MLIs in the EM dataset, CC-MLI synapses were observed in 10% of paired recordings. This may be because MLIs are planar

cells, and our recordings were from surface cells. Consequently, the part of the axon that would contact surface MLIs would often be severed, and paired recordings would tend to underestimate the prevalence of CC to MLI connections.

Gap junction coupling can provide another important means of cell-to-cell communication. In the cerebellar cortex, MLI1s are electrically coupled to each other[34], as are Golgi cells[35]. Both cell types express *Gjd2*, and spikelets characteristic of electrical coupling are observed in intracellular recordings[10]. We never saw such spikelets in recordings from CCs, and PLI1s do not express *Gjd2*[10], which suggests that they are not electrically coupled to other cells.

The observation that CCs rarely inhibit PCs but inhibit many MLIs, raised the possibility that the primary role of CCs may be to regulate MLI inhibition of PCs. MLIs are spontaneously active and are the primary source of inhibition to PCs. Therefore, any change in MLI firing will indirectly influence PCs. We tested the hypothesis by increasing CC firing while simultaneously recording spontaneous inhibition in nearby PCs (Fig. 7A). These recordings were conducted in the absence of blockers, so the large spontaneous IPSCs are outward, and small excitatory EPSCs are inward. In an example pair, elevating CC firing to 97 Hz for 5s markedly decreased spontaneous inhibition in a nearby PC (Fig. 7Ba). The firing of single CCs to an average of 60 spikes/s decreased IPSC charge by an average of 24±5% (Fig. 7C). Thus, a single CC can powerfully disinhibit nearby PCs.

DISCUSSION

We show that CCs represent an unexpectedly large population of interneurons that are present in all lobules of the cerebellar cortex. CCs are highly excitable and receive inputs from all processing stages, including MFs, granule cells, and PCs. CCs in turn inhibit MLIs. Because of their unique position within the cerebellar circuit, CCs are predicted to be critical elements for cerebellar processing.

CCs are a distinct population of cells

Whether CCs constitute a distinct cell type was very much an open question. The initial study of CCs described a cerebellar interneuron with a morphology that differed from PCs, Golgi cells, UBCs and granule cells. Although CCs are similar to MLIs, in that their dendrites and axons are largely restricted to a sagittal plane of the molecular layer, the morphology of CCs differs in important ways. CC dendrites often extend into the granular layer, which is not the case for MLIs. In addition, MLIs with cell bodies near the PC layer tend to make distinctive basket cell synapses onto the soma and axon of PCs, whereas CCs do not. However, the possibility remained that CCs might be an MLI subtype. The relationship of CCs to other PLIs, namely globular cells and Lugaro cells, was unknown.

It is remarkable that despite their identification twenty-eight years ago, subsequent studies failed to provide any insight into the properties and connectivity of CCs within the cerebellar circuit. Several factors hindered the study of CCs. Even though they are abundant relative to PCs and Golgi cells, their presence is obscured by the much more numerous and similarly sized granule cells that are located nearby. Similarly, the application of single cell

molecular approaches to the study of the CCs had also been limited by granule cells vastly outnumbering most other cell types, especially interneurons[36]. We overcame this challenge by transcriptionally profiling 780,553 nuclei, which allowed us to identify three populations of PLIs. Nonetheless it was not possible to link the molecular properties of PLIs to CCs until we found that neurons matching the original description of CC morphology were labelled in Oxtr-Cre × Ai14 mice (Fig. 1AB, Extended Data Fig. 1A). This allowed us to fill cells to determine their morphology, electrophysiological properties, and synaptic connections, and to link these properties to their molecular identity.

Our analyses of differential gene expression showed that CCs are molecularly distinct from MLIs, Golgi cells and PLI3 (Fig. 2B,D,E), but that there are some similarities in the molecular properties of CCs and PLI2. This degree of molecular similarity is comparable to that of MLI1 subtypes (Fig. 2D,E). Nonetheless there is a rather sharp distinction in the expression of *Slc6a5*, suggesting that PLI2 cells release both glycine and GABA, but CCs exclusively release GABA. Oxtr-Cre mice allowed us to target CCs, rather than glycinergic globular cells. CCs and globular cells have similarities and differences. Both are located near the PC layer, although the locations of CC somata extend slightly into the molecular layer, and globular cells into the granular layer. Globular cells and CCs are both inhibited by PCs (Fig. 5). However, CCs and globular cells have distinct dendritic and axonal morphologies, with CC axons ascending locally in a sagittal plane whereas globular cell axons extend in a transverse orientation[25, 26, 37]. Additionally, CCs have much higher input resistances and are more excitable than globular cells[26]. Thus, differences in gene expression, morphology and electrophysiological properties indicate that CCs constitute a distinct type of cerebellar interneuron.

It is important to recognize that even with the addition of the CC as a distinctive type of inhibitory interneuron, the circuitry of the cerebellar cortex is comprised of a small number of cell types. A recent transcriptomic analysis identified just eight types of inhibitory interneurons in the cerebellar cortex: MLI1 (MLI1_1 and MLI1_2 subtypes), MLI2, Golgi1, Golgi2, CC, PLI2, and PLI3[10]. This contrasts with other brain regions, for example 42–59 distinct GABAergic types in M1 cortex[12–14], and 20 GABAergic interneurons in area CA1 of the hippocampus[38, 39]. This suggests that the characterization of a new type of interneuron in the cerebellum is of particular significance.

CCs are widespread and prevalent

CCs are ubiquitous and numerous. Our smFISH results show that CCs are present in all lobules, and our transcriptional profiling identified CCs in all of 16 regions of the cerebellar cortex that were sampled (Extended Data Fig. 4). We found that there were approximately 80% as many CCs as there were Golgi1 cells (based on smFISH). Moreover, CCs are the most abundant PLI with approximately 43% more CCs than globular cells (based on smFISH).

Candelabrum cells within the cerebellar circuit

CCs are inhibited by both PCs and MLIs. Paired recordings established that PC inputs can be particularly powerful, with a single PC accounting for up to 42% of the total spontaneous

inhibitory events in a CC (mean=16%). Although we observed MLI to CC synapses, in comparison to PC-to-CC synapses they were less frequent (3.5% vs 7.3% of pairs), about one quarter the size (3.0 pA vs 11.2 pA mean STA size), and accounted for a much smaller fraction of inhibitory events in CCs (3.1% vs 16%). Together, these findings suggest that PCs are the primary source of inhibition to CCs and that a modest number of PCs powerfully inhibit each CC. However, despite strong trends, with only three connected MLI-to-CC pairs, the differences are not statistically significant.

CCs receive extensive excitatory inputs from many granule cells, as expected for a neuron with dendrites in the molecular layer. We also found that MFs provide rapid short latency excitation. This was somewhat surprising, because MFs are generally thought to be restricted to the granular layer, and CC dendrites only extend slightly into the granular layer. Serial EM reconstruction revealed that CCs receive input from multiple MFs (Fig. 4F, Extended Data Fig. 8) in the form of glomerular and extraglomerular synapses.

Our electrophysiological and molecular studies established that CCs are GABAergic cells that lack a glycine component. This is consistent with the observation that CCs lack *Slc6a5* that encodes the glycine transporter Glyt2, and that is expressed by glycinergic neurons such as globular cells, Lugaro cells and Golgi cells[21]. CCs primarily target MLIs, but make very rare synapses onto other cell types.

Possible functional relevance and significance

CCs are part of a primarily unidirectional inhibitory loop comprised of PCs, CCs and MLIs that has intriguing properties (Fig. 7D,E). Whenever the firing rate of any element in the loop is altered, this circuit will counteract that change in firing rate. In addition, such ring oscillators with an odd number of elements have been studied extensively as a means of generating oscillations that in some cases decay exponentially in amplitude[40, 41]. The nature and duration of these oscillations depend on many factors. Functionally, ring oscillators have the potential to allow a circuit of exclusively inhibitory neurons to generate oscillations, and such a circuit also has the potential to generate undesirable epileptiform activity. Transient cerebellar oscillations sometimes precede specific actions, and can be coincident with oscillations in other brain areas, like motor cortex. It has been proposed that gap-junction coupled Golgi cells could enable such oscillations[42]. The circuit properties we describe here for CCs suggest that they could also generate functionally-relevant oscillations following MFs and granule cell activation and engagement of the CC to MLI to PC loop.

Their synaptic inputs and outputs set CCs apart from the better characterized Golgi cells and MLIs (Fig. 7D). CCs are excited by MFs and granule cells, powerfully inhibited by PCs, and they directly inhibit cells in the molecular layer. Although Golgi cells are also excited by granule cells and MFs, Golgi cells don’t synapse onto cells in the molecular layer and are not inhibited by PCs. MLIs inhibit cells in the molecular layer and some are inhibited by PCs, but MLIs are not excited by MFs. Thus, only CCs simultaneously sample multiple stages of cerebellar processing, including the MF inputs, PC outputs and granule cells. CCs are therefore important circuit elements positioned within the circuit if the cerebellar cortex to weigh the activity of inputs, outputs and within the cerebellum to control the output of the cerebellar cortex.

CCs and other PLIs have some similarities and some differences with regard to connectivity. PCs also strongly inhibit Lugaro cells and globular cells, which is not surprising given that both cell types reside near the PCL where PC collateral synapses are abundant. Stimulation of the granular layer evoked depressing responses in globular cells, which may reflect MF inputs[26]. Light level immunofluorescence also suggested that Lugaro cells receive MF inputs[43] and suggest that they may also inhibit nearby molecular layer interneurons. However, Lugaro cells differ from CCs in that they powerfully inhibit Golgi cells with glycinergic/GABAergic synapses, whereas CC to Golgi cell synapses are exceedingly rare. In addition, Lugaro cells and globular cells have much longer axons than CCs that allow them to influence targets at much further distances than CCs. Thus, CCs and other PLIs have some common circuit properties and some unique specializations, but a more complete comparison is not possible until more is learned about Lugaro cells and globular cells connectivity.

CCs can exert a large influence on PC excitability, and can be thought of as master regulators of PC excitability that are privy to input, output and intrinsic activity. We have shown that a single CC can dramatically alter the inhibition that PCs receive from MLIs, with up to a 60% reduction of inhibitory charge (Fig. 7). EM reconstructions confirmed the physiology experiments, but also revealed that CCs inhibit the majority of nearby MLIs. Granule cells and MFs promote CC firing, reduce MLI firing and disinhibit PCs. This is countered by the activity of PCs themselves, which will have the opposite effect. When PC firing is elevated, it will decrease the firing of CCs that in turn increases the firing of MLIs, thereby resulting in negative feedback to the PC that counteracts the increase in CC firing. These properties, along with the observation that CCs are abundant and widespread, indicate that the properties of CCs must be considered in order to fully appreciate the manner in which the cerebellar cortex functions and contributes to behaviors.

MLI activity regulates calcium signaling in PC dendrites, long-term plasticity of granule cell synapses, and cerebellar learning[44]. This suggests that elevated CC activity, and the resulting suppression of MLI firing, may put the cerebellar circuit and PCs in a state that promotes long-term depression (LTD) of granule cell synapses and cerebellar learning.

Ultimately, the behavioral roles of CCs will need to be determined with *in vivo* studies. The first step will be to examine the activity of CCs during behavior. Calcium signals may be possible using the Oxtr-Cre mice, but it is not clear that they will have sufficient temporal resolution. Single unit recording promises to be challenging because of the close proximity of CCs to the PC layer where large ongoing PC spiking will make it difficult to isolate CC spiking. Perhaps guided patch recordings will be required, but this will be challenging for these small cells. The most promising means of determining the behavioral roles of CCs is to optogenetically activate or suppress CC firing during behavior. Although the MLI and PC contamination makes the Oxtr-Cre mice inappropriate for this application, in the future, an intersectional genetic strategy should allow selectively targeting of CCs, and lead to new insights into their function.

METHODS

ANIMALS

Animal procedures have been carried out in accordance with the NIH and Animal Care and Use committee (IACUC) guidelines, and protocols approved by the Harvard Medical School and Broad Institute Standing Committee on Animals.

C57BL/6 mice were obtained from Charles River Laboratories and used for smFISH experiments. For all other experiments, we used the Oxtr-cre mouse line (036545-UCD; STOCK Tg(Oxtr-cre)ON66Gsat/Mmucd, from MMRRC) crossed with the ai14 reporter mouse line and kept in a C57BL/6 genetic background. Animals of either sex aged 28–45 days were randomly selected for experiments.

Animals were housed on a normal light-dark cycle with an ambient temperature of 18–23 °C with 40–60% humidity

Electrophysiology

Slice preparation—Juvenile animals of either sex aged 28–45 days old were anesthetized with an intraperitoneal injection of ketamine (10 mg/kg) and then perfused transcardially with ice cold cutting solution containing (in mM) 110 CholineCl, 7 $MgCl_2$, 2.5 KCl, 1.25 NaH_2PO_4, 0.5 $CaCl_2$, 25 Glucose, 11.5 Na-ascorbate, 3 Na-pyruvate, 25 $NaHCO_3$, equilibrated with 95% O_2 and 5% CO_2. The brain was rapidly dissected, and the cerebellum was cut into 250 μm thick parasagittal slices in the same solution on a vibratome (VT1200S, Leica). Slices were then transferred to 34°C warm artificial cerebrospinal fluid (ACSF) containing (in mM) 125 NaCl, 26 $NaHCO_3$, 1.25 NaH_2PO_4, 2.5 KCl, 1 $MgCl_2$, 1.5 $CaCl_2$, and 25 glucose, equilibrated with 95% O_2 and 5% CO_2 and incubated for 30 min. Slices were then stored at room temperature until recording for up to 6 hours.

Recordings—CC, MLI and PC recordings were performed at ~32 °C with an internal solution containing (in mM) 150 K-gluconate, 5 KCl, 10 HEPES, 10 MgATP, 0.5 NaGTP, 5 phosphocreatine-$tris_2$, and 5 phosphocreatine-Na_2, and 0.1 Alexa 594 (pH adjusted to 7.2 with KOH, osmolality adjusted to 310 mOsm/kg). The chloride reversal potential was adjusted to −85 mV. Visually guided whole-cell recordings were obtained with patch pipettes of ~4 MΩ resistance pulled from borosilicate capillary glass (BF150–86-10, Sutter Instrument, Novato, CA). Electrophysiology data was acquired using a Multiclamp 700B amplifier (Axon Instruments), digitized at 20 kHz and filtered at 4 kHz with mafPC (freeware package written in Igor Pro 8 (Wavemetrics,Lake Oswego, OR) by M. Xu-Friedman, latest version 10/30/2019). For isolating inhibitory synaptic currents in voltage clamp and the following receptor antagonists were added to the solution (in μM): 2 R-CPP, 5 NBQX, 1 strychnine, 1.5 CGP. All drugs were purchased from Abcam (Cambridge, MA) and Tocris (Bristol, UK). To obtain an input-output curve, CCs were injected with a constant hyperpolarizing current to hold them at ~−65 mV, and 500 ms long current steps ranging from −30 pA to +30 pA were injected in 5 pA increments. Capacitance and input resistance (Ri) were determined using a 10 pA, 50 ms hyperpolarizing current step. Spontaneous firing rate and resting membrane potential were determined using cell-attached recordings

in voltage clamp mode. To determine V_m, a series of voltage ramps from +100 to −120 mV were averaged, and the reversal potential of the leak current was calculated by the interception of a linear fit to the leak current and the voltage activated potassium current [45]. For the experiments in Fig. 7, CC firing was evoked in loose-patch mode in voltage clamp by stepping the pipette voltage to positive values (range +70 to +150mV). To determine the AMPA/NMDA ratio, we stimulated GrC axons in the molecular layer and recorded EPSCs in CCs during a voltage step to +40mV in the presence of inhibitory synaptic blockers. Each stimulus trial was accompanied by a voltage step to +40mV without stimulation. This was used for subtracting voltage dependent and leak currents.

We characterized the contributions of AMPARs and NMDARs to granule cell to CC synaptic currents by using holding potential and pharmacology. We used theta glass stimulation (100μs 140–250 μA) of the molecular layer to evoke granule cell inputs and recorded EPSCs from CCs at −65 mV and at +40 mV with a Cs based internal solution (in mM, CsF: 35, CsCl: 110, Hepes: 10, EGTA: 10 and QX314: 2). We then blocked the AMPA component with NBQX (5μM), and followed this by bath application of the NMDAR antagonist CPP (2μM). Current traces are the average of approximately 10 trials. For some cells, where the AMPA and NMDA components were clearly separated, we used the peak amplitudes of the fast and slow components as a measure of the $AMPA_R$ and $NMDA_R$ mediated currents, respectively.

For measurement of the chloride reversal potential, we recorded CCs in the presence of NBQX, CGP, CPP and strychnine using gramicidin perforated patch. We recorded spontaneous IPSCs at voltages between −95mV and-60mV, measured the sIPSC charge for each voltage and calculated the reversal of the sIPSC charge. Traces were low-pass filtered with a Savitzky-Golay filter (order 3, frame= 501) and slow fluctuations were removed by subtracting a median filtered version of each trace (kernel=10000=0.5s) prior to sIPSC charge measurement. The internal solution was, in mM: 110 K-methanesulfonate, 13 NaCl, 2 $MgCl_2$, 10 EGTA, 1 $CaCl_2$, 10 HEPES, 2 QX314 and 10 μg/ml of Gramicidin A (Sigma-Aldrich).

For the measurement of fraction of inhibitory events in Fig. 5D, we calculated the number of events time-locked to the presynaptic spike of spontaneously active PCs and MLIs and divided it by the total number of spontaneous IPSCs in CCs. CCs have a high rate of sIPSCs, therefore, the number of IPSCs attributed to a connected presynaptic cell was corrected for the baseline rate of spontaneous inhibition using the baseline of a peri-spike time histogram of the sIPSCs.

For measurement of climbing fiber spillover currents, we recorded CCs or MLIs in voltage clamp in the Oxtr-cre × Ai14 mouse at −65mV. The recordings were made at elevated external calcium (2.5 mM), to allow comparison with previous studies of climbing fiber spillover [29, 31], and in the presence of gabazine, CGP and Strychnine. We used a Cs based internal solution (in mM, CsF: 35, CsCl: 110, Hepes: 10, EGTA: 10 and QX314: 2) for these recordings.

We used a theta glass stimulus electrode to stimulate the granule cell layer with pairs of stimuli (100μs duration, 50ms ISI) at different locations in an area ~50μm into the granule cell layer and ~100 μm on each side of the soma of the cell being recorded. We recorded an average of 23 sites per cell in search of inputs with slow kinetics and a marked paired pulse depression (PPR <0.6). We then characterized these inputs by doing a stimulus intensity curve, from 40μA to 140μA in 20μA increments to evaluate the all or none nature of the response (10 s, ITI, 4 trials per intensity), followed by 20 single stimuli, which were used for analyzing the kinetics and amplitude of responses. Finally, we bath applied DL-TBOA (50μM) while stimulating the input (10s ITI, single stimuli) at a stimulus intensity of 140μA. Traces shown are averages of >10 trials for baseline and in the presence of TBOA.

For analysis of the decay kinetics, we fit a double exponential function to the decay of the mean EPSCs [30]. We report the time constant of the fast component (Extended data Fig. 7C,D).

Statistics and Reproducibility

Acquisition and analysis of electrophysiological data were performed using custom routines written in MATLAB (Mathworks, Natick, MA) and IgorPro (Wavemetrics, Lake Oswego, OR). Data are reported as median ± interquartile range for box plots; whiskers, up to 1.5x interquartile range, and as mean for bar graphs, and statistical analysis was carried out using the Wilcoxon signed rank test as indicated. For Figure 1F a Poisson generalized linear mixed effect model of the form SpikeCount ~ 1 CurrentSteps*CellType with a canonical log link function wasfitted using maximum pseudo-likelihood estimation, and the coefficients were tested with a two-sided unpaired t-test without multiple comparison correction. To compare the proportions of connected MLI-CC and PC-CC pairs for Figure 5, a two-sided Chi-squared test with Yates continuity correction was performed. Statistical significance was assumed at $p < 0.05$ and P values and n are stated in the figure legends.

The number of cells, mice and summary of electrophysiological parameters are presented in supplementary table 1 and 2. Micrograph shown in Figure 1A is a representative example of the expression pattern seen in >100 Oxtr-cre × ai14 mice. 2-photon images like the ones shown in Figure 1B and Extended Data Figure 1A,D were obtained for 27 cells from 16 mice and similar results were obtained. Micrographs and average smFISH signals like the ones shown in Figure 3A,B,F,G and Extended Data Figure 2A,B were obtained for >1000 cells in each category (exact n is shown in Figure3E,J). This data was obtained from 8, 40μm thick sagittal cerebellar slices from 1 male and 1 female mouse for wild type experiments (Extended Data Figure 3) and for 4, 40μm thick sagittal cerebellar slices in 1 female Oxtr-cre × ai14 mouse (Extended Data Figure 5). Experiments showing EM reconstructions, such as the ones in Figures 4F, 5E, 6I and Extended Data Figures 8, 9 and 10 were replicated in the 4 most completely reconstructed Candelabrum cells from 1 mouse with the same result. Only selected synapses and synaptic partners are shown for clarity.

No statistical methods were used to predetermine sample sizes. Sample sizes reflect those standardly used in the field and in our previous studies. Data met the assumptions of the statistical tests used. Normality and equal variance were not tested, and non-parametric tests were used where applicable. Cell selection of tdTomato positive cells for smFISH analysis

was done blind to the expression of smFISH probes. For all other experiments, blinding does not apply since only one group was studied. No data or animals were excluded from this study.

2-photon imaging and analysis

CCs were filled with 100μM Alexa-594 through the patch pipette to visualize their morphology using 2-photon imaging. We used a custom-built 2-photon laser scanning microscope with a 40X water immersion objective (Olympus, 0.8 NA) and a pulsed 2-photon laser tuned to 800 nm (Mira 900, Coherent, Santa Clara, CA). Data was collected using ScanImage, running on Matlab R2009b. We acquired Z-stacks with 1 μm Z-step of Alexa-594 fluorescence and L-DIC. 2 photon images were processed in ImageJ 1.53c to create maximum intensity Z projections of Alexa-594 fluorescence which were subtracted from a single DIC focal plane.

For morphological analysis of 2-photon images, we registered the 2-photon 3D stacks to a reference image (Extended Data Fig. 1B) with a nonreflective similarity transformation, which used 2 control point pairs: one in the middle of the Purkinje cell layer and one in the pia, in line with the soma. This was done to create the same orientation and to align the circuit layers. This transformation preserves shapes and only uses rotation, scaling and translation. We then manually segmented the axon, dendrites and soma in ImageJ 1.53c using masks in the max Z-projection, which were subsequently refined in 3D. The location of all axon boutons was manually labeled in 3-D and analyzed in Matlab R2019b (Mathworks).

Floating Slice Hybridization Chain Reaction

Tissue preparation—Male/female p44–45 mice were anesthetized with an intraperitoneal injection of ketamine (10 mg/kg) and transcardially perfused with ice-cold PBS, followed by ice-cold 4% PFA in PBS. Brains were post-fixed overnight in 4% PFA at 4 °C, washed in PBS, then sliced sagittally at a thickness of 40μm using a vibratome (VT1000S, Leica) and transferred to a solution of 70% ethanol in RNAase-Free water until HCR was performed.

HCR—A floating slice HCR protocol was performed (based on dx.doi.org/10.17504/protocols.io.bck7iuzn) with the following HCR probes and hairpins from Molecular Instruments, Inc. (Los Angeles, CA): Neurexophilin 1 (*Nxph1*), Aldehyde dehydrogenase 1 family, member A3 (*Aldh1a3*) and Sodium-and chloride – dependent glycine transporter 2 (*Slc6a5*). Amplification hairpins were B1–647 (Alexa-647), B2–488 (Alexa-488) and B3–546 (Alexa-546).

Imaging—Slices were mounted on a glass slide with ProLong Glass mounting medium without DAPI (ThermoFisher Scientific) and imaged on a widefield slidescanner (Olympus VS-ASW-L100) using a 40X air objective (Olympus, 0.95 NA) and a 16-bit camera (Hamamatsu Orca-R^2 model C10600) with 7–11 focal planes (3μm per Z plane) per channel and automatic tiling. Focusing was done manually for ~100 focal reference points throughout each slice. The fluorescence filter sets used were FITC (Chroma #39002), ET-CY3/TRITC (Chroma # 49004) and Cy5 (Chroma # 39007).

Image processing—Image processing was done in Matlab R2019b (Mathworks), unless otherwise specified. Background fluorescence was reduced by subtracting a median filtered version for each individual focal plane (kernel size= 20 × 20 px). After this, puncta were detected using Fast 2D peak finder (Matlab central file exchange, Natan 2020) with a threshold determined by the median absolute deviation of the image, then masked with a circular kernel (radius= 10px) and Z projected as a maximum intensity projection. Each channel was processed separately.

Max Z projections were downscaled to half resolution and registered to a reference slice using a geometric transformation fit to control point pairs (4^{th} order polynomial transformation). Control points were manually selected along the PCL and edge of the molecular layer.

Subsequently, a mask was created for each registered channel by applying a maximum filter (circular kernel, radius= 5 px), followed by a 2D Gaussian filter (sigma=8 px) and manual thresholding. Mask combinations were used to create cell type masks (e.g., *Nxph1*-mask ∧ *Aldh1a3*-mask ∧ *Slc6a5*−mask = globular cell mask), which were used on the background subtracted Z projections. Images masked for each cell type mask were used to manually label the location cells in the slice in ImageJ 1.53c.

Background fluorescence for the *Nxph1* channel was used to create polygons that delineate the edge of the molecular layer and the PC layer, which were used to measure the distance of each cell to the PCL and Pia. For computing the density of cells in each lobule (Fig. 3D), cell counts were normalized to the length of the PCL in each lobule. For the layer distribution histograms (Fig. 3E), cell counts were normalized to the number of slices counted.

In experiments with Oxtr-Cre × Ai14 mice, crosstalk signal originating from tdTomato fluorescence was corrected by subtracting a scaled version of the tdTomato channel from the *Slc6a5* and *Aldh1a3* channels prior to puncta detection. The scaling factor was determined by the average ratio of tdTomato/*Slc6a5* or tdTomato/*Aldh1a3* pixel values from regions in the molecular layer that expressed tdTomato but were devoid of fluorescent puncta. The filter set used to image tdTomato has center wavelengths that excite tdTomato (up to 29% of peak excitation) and allow the left tail of the emission spectrum to pass (up to ~18% of peak emission intensity).

snRNA-seq

snRNA-seq data for cerebellar interneurons was obtained in Kozareva et al. 2021. Briefly, high throughput single-nucleus RNA-seq (snRNA-seq) was used to analyze 780,553 nuclei isolated from 16 different lobules from 6 p60 mice. Of these, 1177 were categorized as CCs, 735 as globular cells, 531 as Lugaro cells, 32716 as MLI1, 10608 as MLI2, 3075 as Golgi1 and 914 as Golgi2.

snRNAseq data clustering was done as previously described [10]. Briefly, cell type annotation was done iteratively using dimensionality reduction, clustering, and removal of cells with high mitochondrial expression using a variation of the LIGER v0.4.2 package [46], which

uses integrative non-negative matrix factorization and Louvain community detection. Gene expression was normalized by the total number of UMIs/cell and scaled for each gene as previously described in Welch et al., 2019. For visualization of clusters, expression data from GABAergic interneuron nuclei (*Gad1/2*+) was merged, preprocessed in a standard way using Seurat V2.3.4 and visualized with UMAP with 25 principal components in R v3.5.3

Pseudotime expression trajectories for cell type comparison analyses were calculated using Monocle 2 v2.10.1[47] and analyzed for continuity as previously described[10].

Notably, even though CCs were labelled in Oxtr-Cre × Ai14 mice, we did not observe any *Oxtr* expression in any neurons in the cerebellar cortex. This suggests that expression in this line arises from either random integration or lack of regulatory elements leading to ectopic expression in cells that do not normally express the gene. This has been widely taken advantage of to target specific cell types, such as newborn hippocampal granule cells in POMC-GFP mice[48, 49].

Serial Electron microscopy

We previously described the procedures of mouse tissue preparation [50], sectioning, collection, and TEM imaging (without post-sectioning staining) [50, 51]. We used an segmentation workflow based on U-Net CNN to automatically generate the neuron boundary and reconstruct the 3D neuron morphologies [52]. To deploy the algorithm across hundreds of workers concurrently, we used the Daisy scheduler (https://github.com/funkelab/daisy). To rapidly reconstruct and correct errors from automated segmentation, we developed and used a proofreading work-flow called Dahlia where segmentation is divided into independent cubes; annotators would then select a fragment of a neuron and grow it into the adjacent block until completion. During each growth step, the neuron was visualized and checked for possible split or merge errors.

EM data was visualized in Neuroglancer and Matlab R2019b.

To identify CCs, we first screened all the small neurons within ± 20μm of the center of the PCL, discarded all the granule cells and MLIs, based on their characteristic morphology and focused on PLIs that matched closely the description of CCs, as well as our 2-photon fills. We restricted our analysis to the most completely reconstructed cells, prioritizing the presence of a beaded axon in the molecular layer. Synapses and cell labels were manually generated. Extended Data Fig. 10 illustrates the importance of using serial EM to identify connections.

DATA AVAILABILITY

snRNAseq data was published in Kozareva et al. 2021 and is accessible at (https://singlecell.broadinstitute.org/single_cell/study/SCP795/) and at the NeMo archive (https://nemoarchive.org/).

Serial EM data is accessible at https://github.com/htem/cb2_data_availabilityData will also be publicly available in the BossDB (https://bossdb.org/) repository upon publication of Nguyen et al. bioRxiv 2021, which describes the EM dataset.

All other data has been added to the Harvard Dataverse, Candelabrum Cell Dataset (https://doi.org/10.7910/DVN/APCCSN)

CODE AVAILABILITY

Analyses used in this study are largely standard approaches for this type of data. The code that supports these findings is available at the Harvard Dataverse https://doi.org/10.7910/DVN/APCCSN And at https://github.com/MacoskoLab/cerebellum-atlas-analysis.

Extended Data

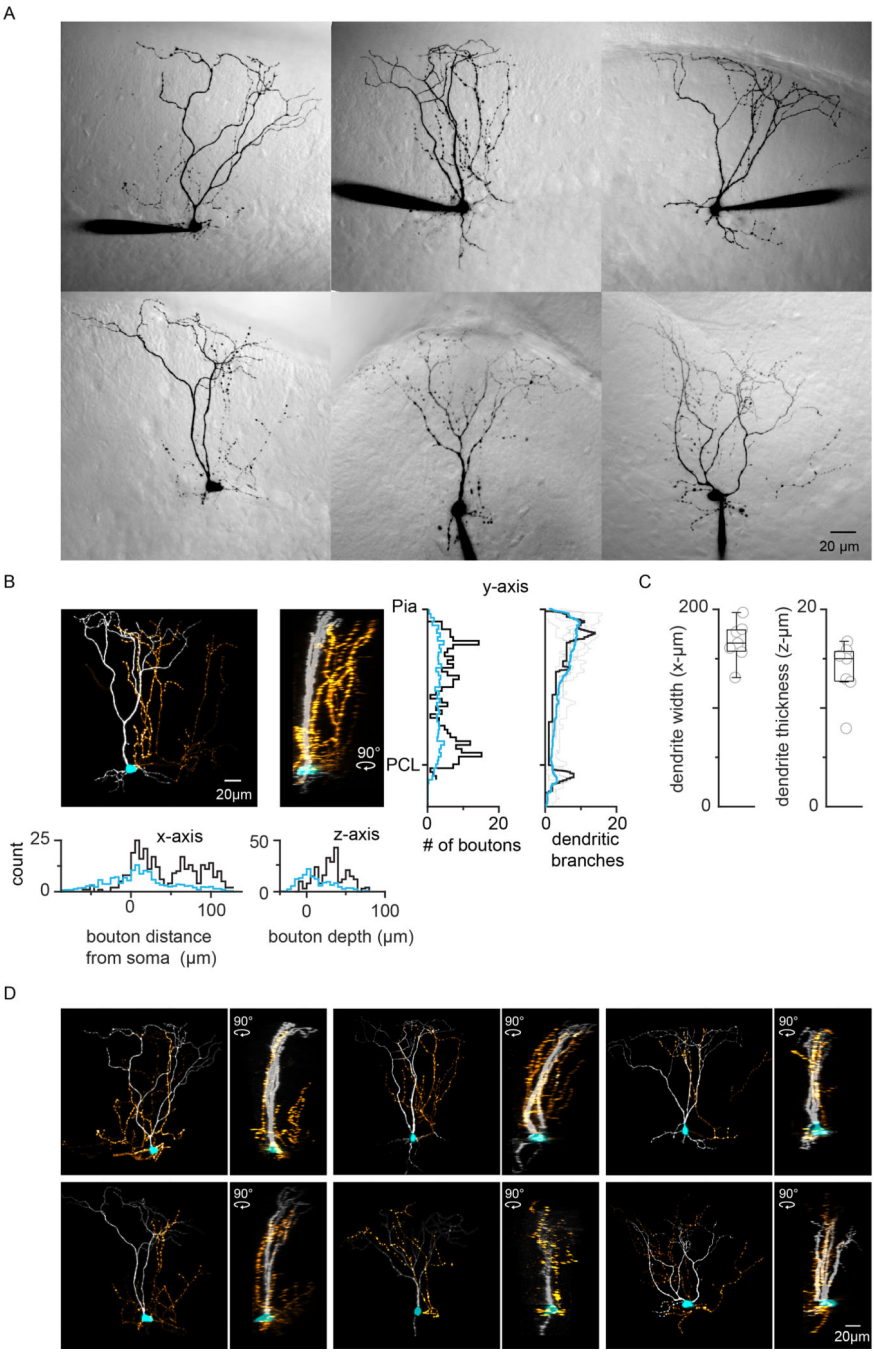

Extended Data Fig. 1. Examples of candelabrum cell morphologies

A. tdTomato-positive CCs filled with an Alexa594-containing patch pipette and imaged using 2-photon microscopy. Images show LS-DIC in gray indicating the cell location in the slice, and Alexa-594 fluorescence in black as a maximum intensity Z-projection.

B. Example of a CC (from A) with the axon shown in yellow, the dendrites in white, and the cell body in cyan. A corresponding sideview is shown, along with quantification of dendritic

branching in the cortical layers and distribution of boutons relative to the cell body (example cell, black. n=305 boutons, average of n=7 cells, light blue. n=1125 boutons).

C. Summary of the dendritic arbor morphology in CCs. In box plots, box outlines and center line indicate median and interquartile range, and the whiskers indicate data points up to 1.5x interquartile range. n=7 cells.

D. Images of the CCs shown in A colored as in B. Side views are also shown for each cell.

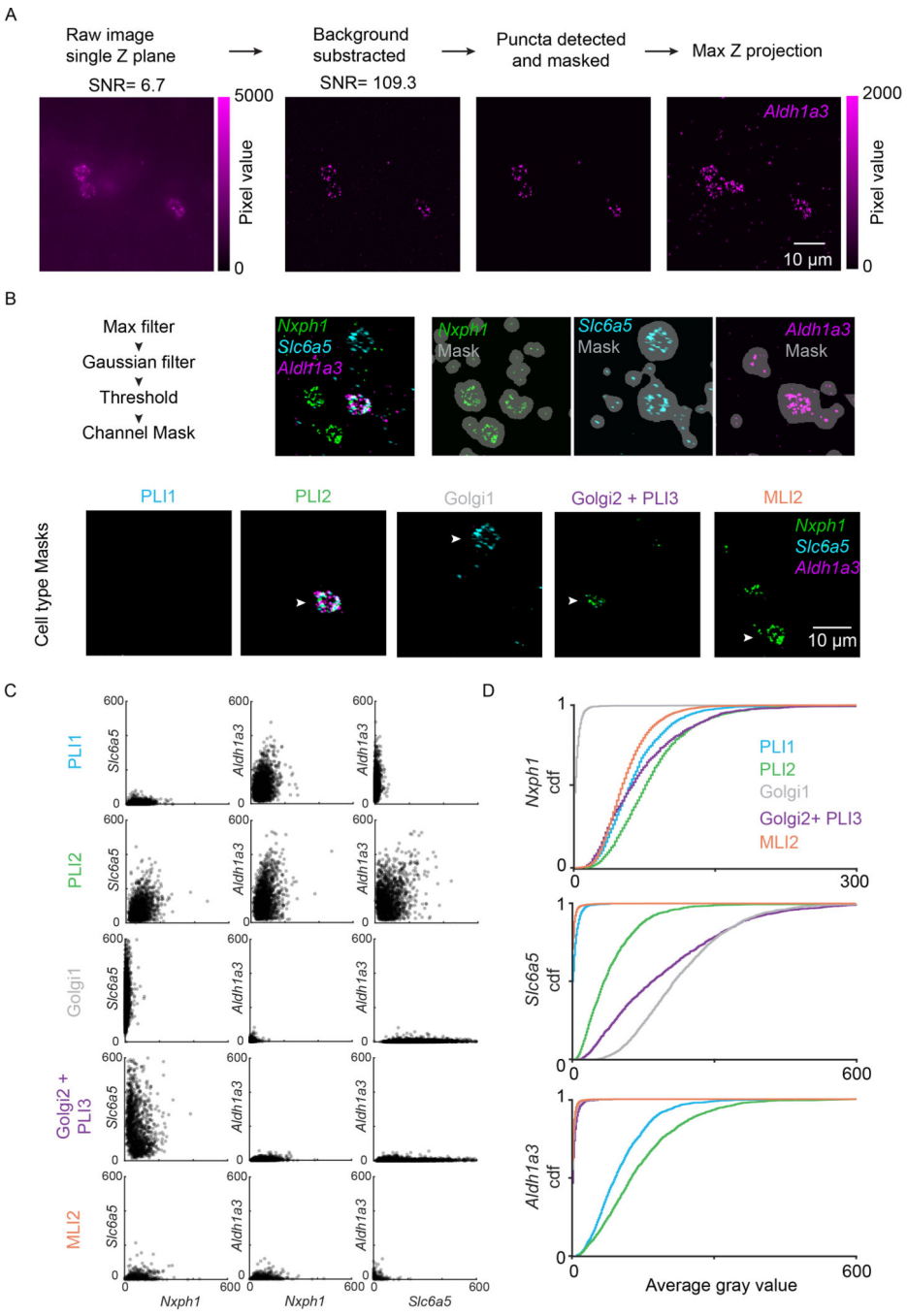

Extended Data Fig. 2. Methods used to analyze FISH data

A. Raw fluorescence image for one channel → image with background fluorescence subtracted → individual puncta are then detected in each slice → the results from all slices in a Z-stack are combined.

B. Top) a mask is created for each channel. Bottom) Channels masks are combined to create cell type masks. Examples for the same field of view are shown for all cell types. Color scales are the same as in Figure 3.

C. Scatter plots of FISH fluorescence are shown for all cells of each cell type.

D. Cumulative histograms are shown for *Nxph1, Slc6a5, Aldh1a3* for the different cell classes.

Extended Data Fig. 3. Summaries of locations of five classes of cells in different slices, as in Fig. 3.

PLI1: light blue *Nxph1*+ *Slc6a5*− *Aldh1a3*+

PLI2: green *Nxph1*+ *Slc6a5*+ *Aldh1a3*+

Golgi1: grey *Nxph1*− *Slc6a5*+ *Aldh1a3*−

Golgi2+ PLI3: purple *Nxph1*+ *Slc6a5*+ *Aldh1a3*−

MLI2: orange *Nxph1*+ *Slc6a5*− *Aldh1a3*−

A. Four slices each from a female (top) and a male (bottom) are shown.

B. The locations of cell types from all slices are overlayed. The symbol sizes have been reduced to allow better visualization of the locations of individual cells. Each type of interneuron displayed a characteristic distribution. The distribution of PLI2s was most similar to that of PLI1s (Fig. 3C–E, **Extended Data Fig. 3**, *green*). PLI2s were clustered around the PCL, although unlike PLI1s they were not present in the molecular layer but extended into the upper part of the granular layer (Fig. 3E, *green*). Golgi1 cells were found in all lobules, and were restricted to the granule cell layer (Fig. 3C–E, **Extended Data Fig. 3**, *grey*). Although our labelling strategy was focused on identifying PLI1s, rather than discriminating between PLI3s and Golgi2 cells, the combined labelling of these two cell types is informative (Fig. 3C–E, **Extended Data Fig. 3**, *light purple*). The density of cells shows a gradient in the different lobules, peaks in lobule IX, and is extremely low in lobule X. The small peak in cells near the PCL likely reflects PLI3s, which are more rare than other PLIs. As expected, MLI2s are present at higher densities than the other cell types and are restricted to the molecular layer (Fig. 3C–E, **Extended Data Fig. 3**, *orange*).

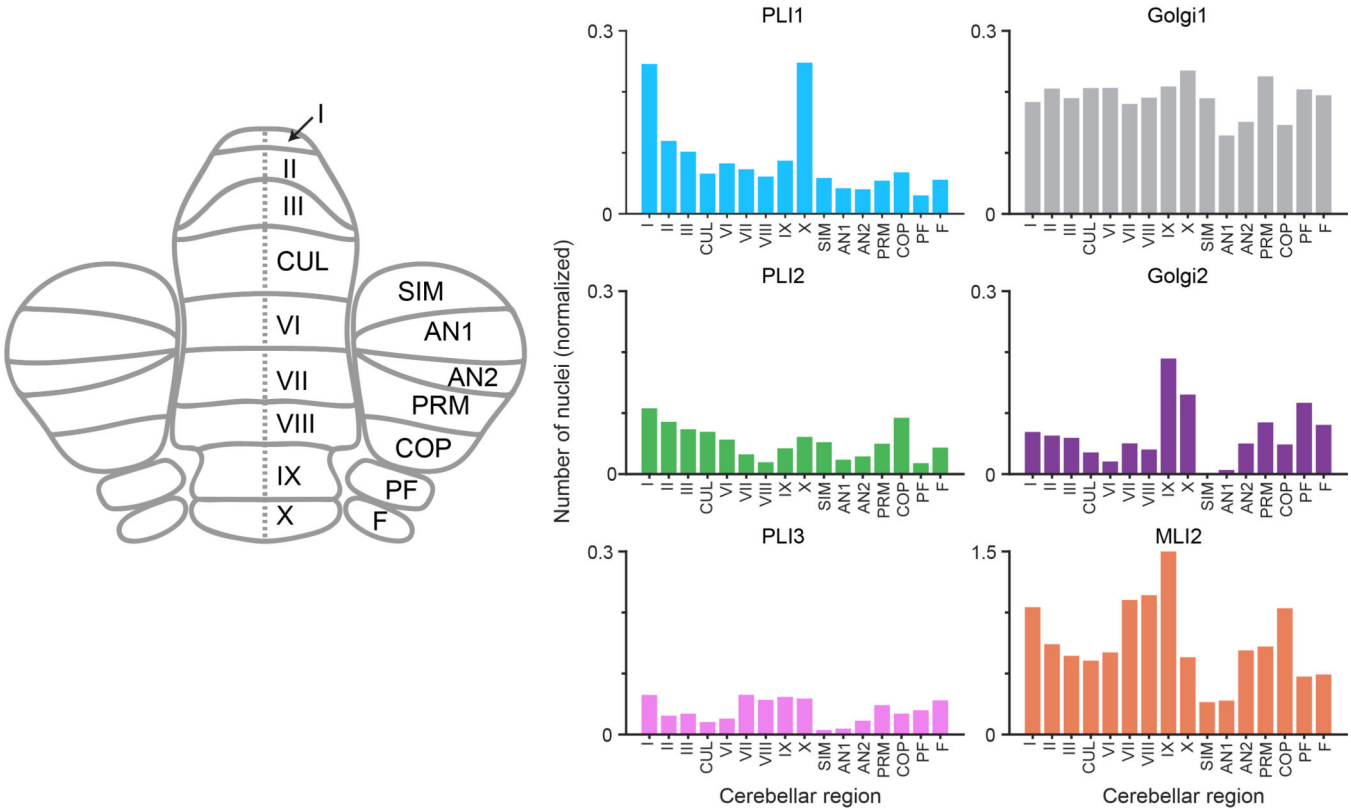

Extended Data Fig. 4. snRNAseq regional nuclei counts

snRNAseq nuclei counts for PLI1, PLI2, PLI3, Golgi1, Golgi2 and MLI2 cells from different regions of the cerebellum. Nuclei counts are normalized to the number of PC nuclei in each region. CUL=Culmen, SIM=lobule simplex, AN1= Crus I of ansiform lobule, AN2= Crus II of ansiform lobule, PRM= paramedian lobule, PF=paraflocculus, F=flocculus. Data are from Kozareva et al. 2021.

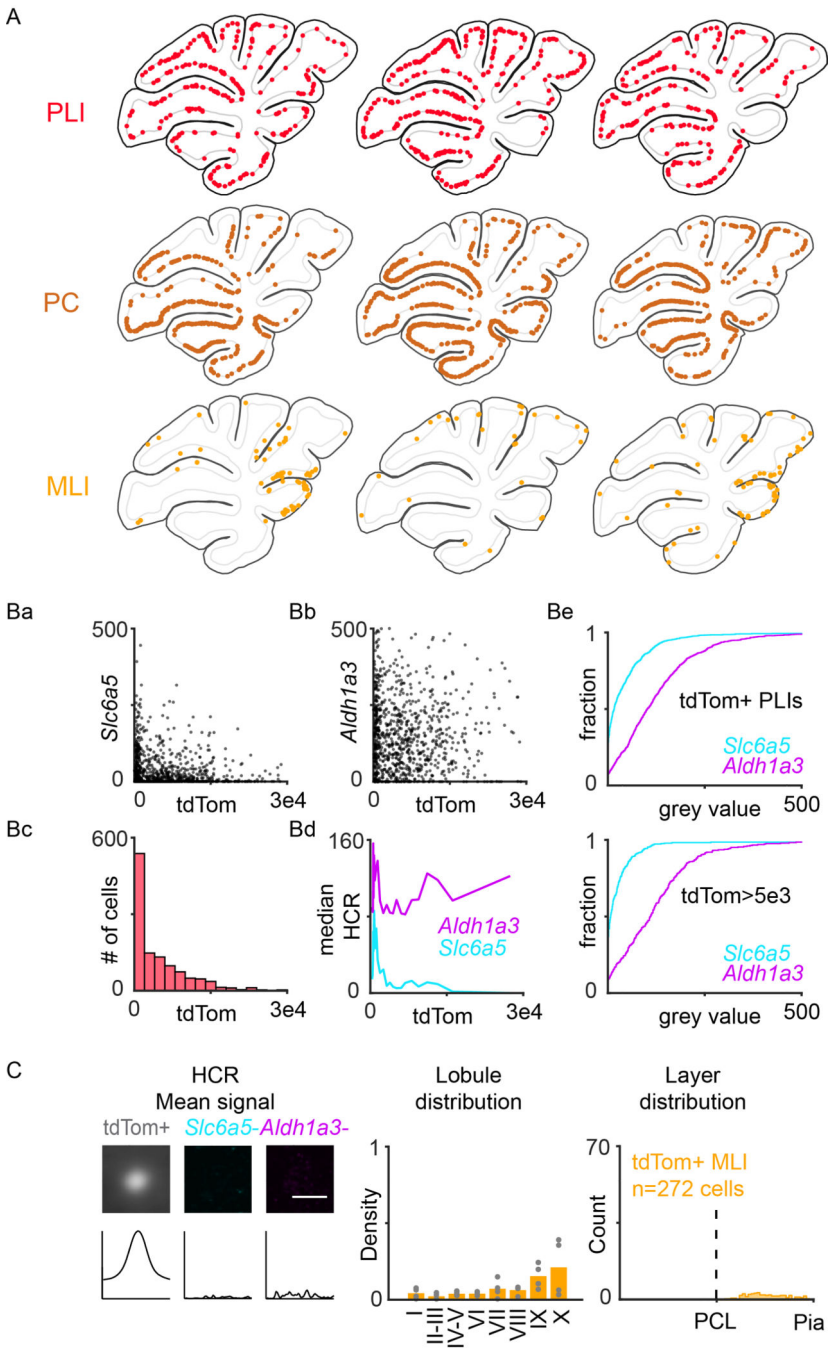

Extended Data Fig. 5. Properties of labelled cells in Oxtr-Cre × Ai14 mice

Slice location of tdTomato labeled cell types for different cerebellar slices. Small PCL cells (top, n=1206 cells), PCs (middle, n=1862 cells) and some MLIs (bottom, n=272 cells) were labeled.

Ba) Scatter plot of *Slc6a5* signal for individual PLIs as a function of tdTomato fluorescence.

Bb) Scatter plot of *Aldh1a3* signal for individual PLIs as a function of tdTomato fluorescence.

Bc) Histogram showing distribution of tdTomato fluorescence intensities in PLIs.

Bd) Median HCR signal for PLIs as a function of tdTomato fluorescence.
Be) Cumulative plots showing distribution of HCR mean values in all tdTomato expressing PLIs (top) and in PLIs with high tdTomato fluorescence (bottom).
Summary showing sparse tdTomato labelling of MLIs in Oxtr-Cre × ai14 mice. MLIs do not express *Slc6a5* or *Aldh1a3*. These cells exist in low density in the most frequent recording regions (lobule VI-VIII). Lobule IX and X were avoided for electrophysiology recordings because they showed the highest density of MLI labeling. n=4 slices.

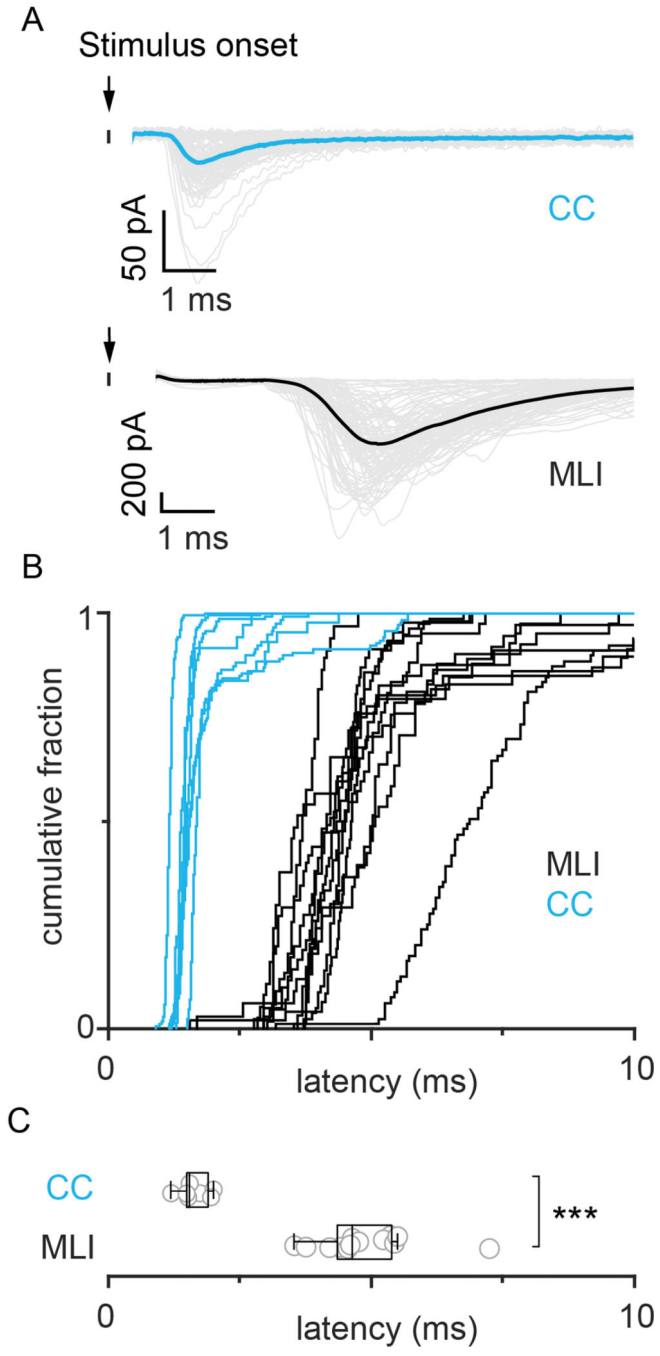

Extended Data Fig. 6. Latency of excitatory inputs elicited by electrical stimulation of the white matter.

A) Example cells aligned to the same timescale as the cumulative plot in B. individual trials shown in gray and averages in light blue (CC) and black (MLI).

B) Cumulative distributions of the latency of the first EPSC after electrical stimulation of the white matter for CCs (light blue) and MLIs (black). Each cell is plotted separately. CC n=7 cells, MLI n=13 cells.

C) Summary of the median latency of EPSCs evoked by white matter stimulation. Each point represents a cell. n=7 CCs and 13 MLIs. p=3.6 e-4, two-sided Wilcoxon rank test. In box plots, box outlines and center line indicate median and interquartile range, and the whiskers indicate data points up to 1.5x interquartile range.

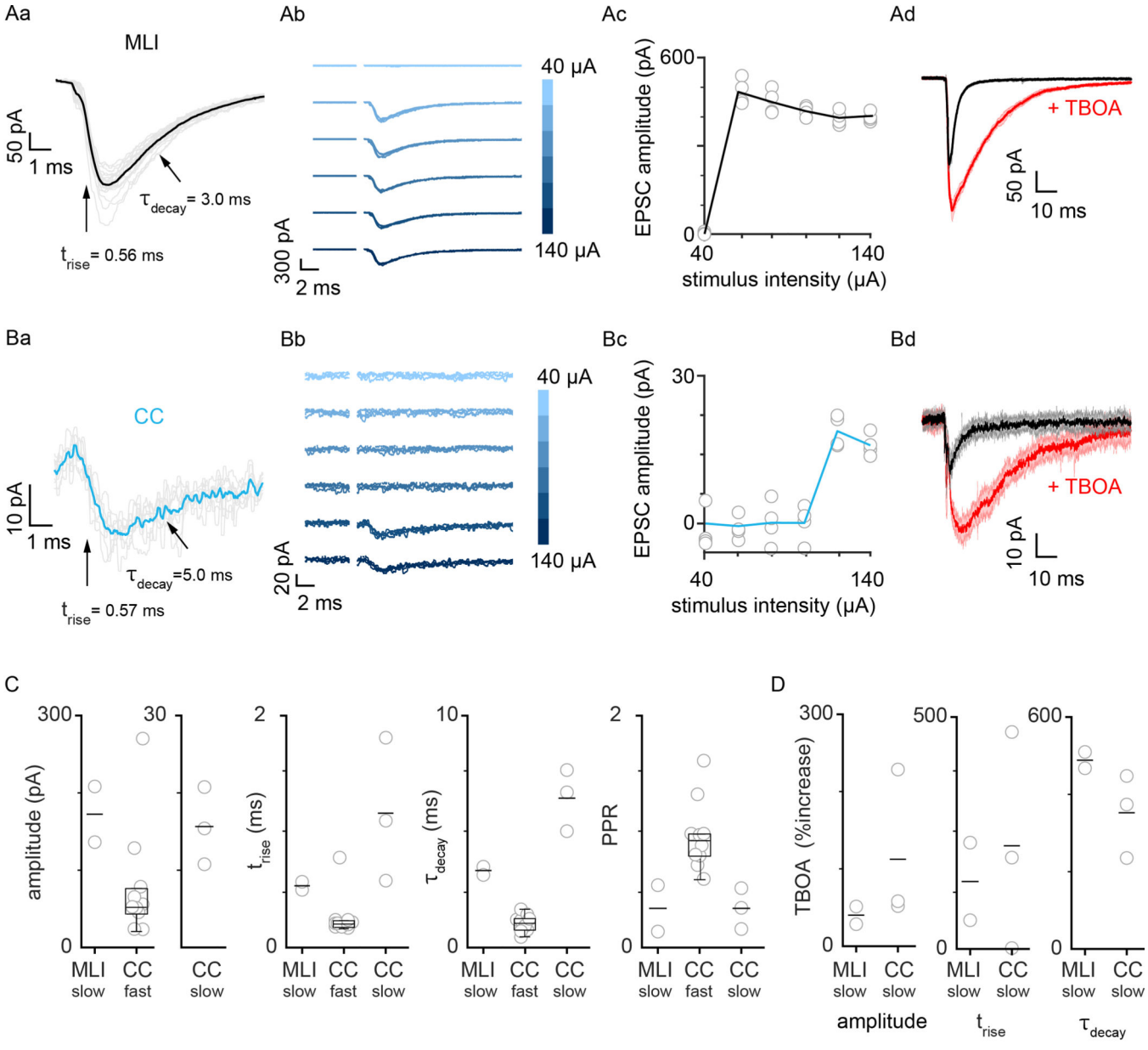

Extended Data Fig. 7. Climbing fibers (CFs) excite candelabrum cells via glutamate spillover

Previous studies have shown that CFs do not synapse directly onto molecular layer interneurons (MLIs), but that CF activation evokes a slow spillover current in MLIs and GCs. We performed similar experiments. We placed a stimulus electrode in the granular layer to activate axons and then assessed the properties of the inputs by stimulating with multiple trials for a range of stimulus intensities, and determining the rise time and decay times of EPSCs. Experiments were performed with inhibitory transmission blocked. As in previous studies, we identified putative CF spillover currents based on slow rise and decay times, all or none activation and pronounced depression. If it satisfied these criteria we went on to determine its sensitivity to inhibiting glutamate uptake with TBOA. Many stimulus sites and many EPSCs were tested for each cell and CF inputs to MLIs were observed in 2 of 4 cells, whereas they were observed in 3 of 25 CCs

Aa) Example of CF spillover excitation for an MLI. Individual traces shown in gray and average in black.

Ab) Responses evoked by a stimulation of increasing intensities for the same MLI, with 4 traces overlaid for each intensity.

Ac) Summary of EPSC amplitudes as a function of stimulus intensity for Ab.

Ad) Slow EPSCs before and after bath application of 50μM DL-TBOA. Shaded error bars show the average +/− SEM for 10 trials.

Ba-d) Same as A for a candelabrum cell.

C. Summary of amplitude, kinetic parameters, and paired pulse ratio for CF spillover excitation onto CCs. n= 2 cells (MLI_{slow}), 3 cells (CC_{slow}) and 10 cells (CC_{fast}).

D. Summary of the effect of TBOA on the amplitudes, rise-times and decay times of synaptic responses. n is the same as in panel C. In all box plots, box outlines and center line indicate median and interquartile range, and the whiskers indicate data points up to 1.5x interquartile range. Whenever n<5, only the mean value is indicated with a horizontal line.

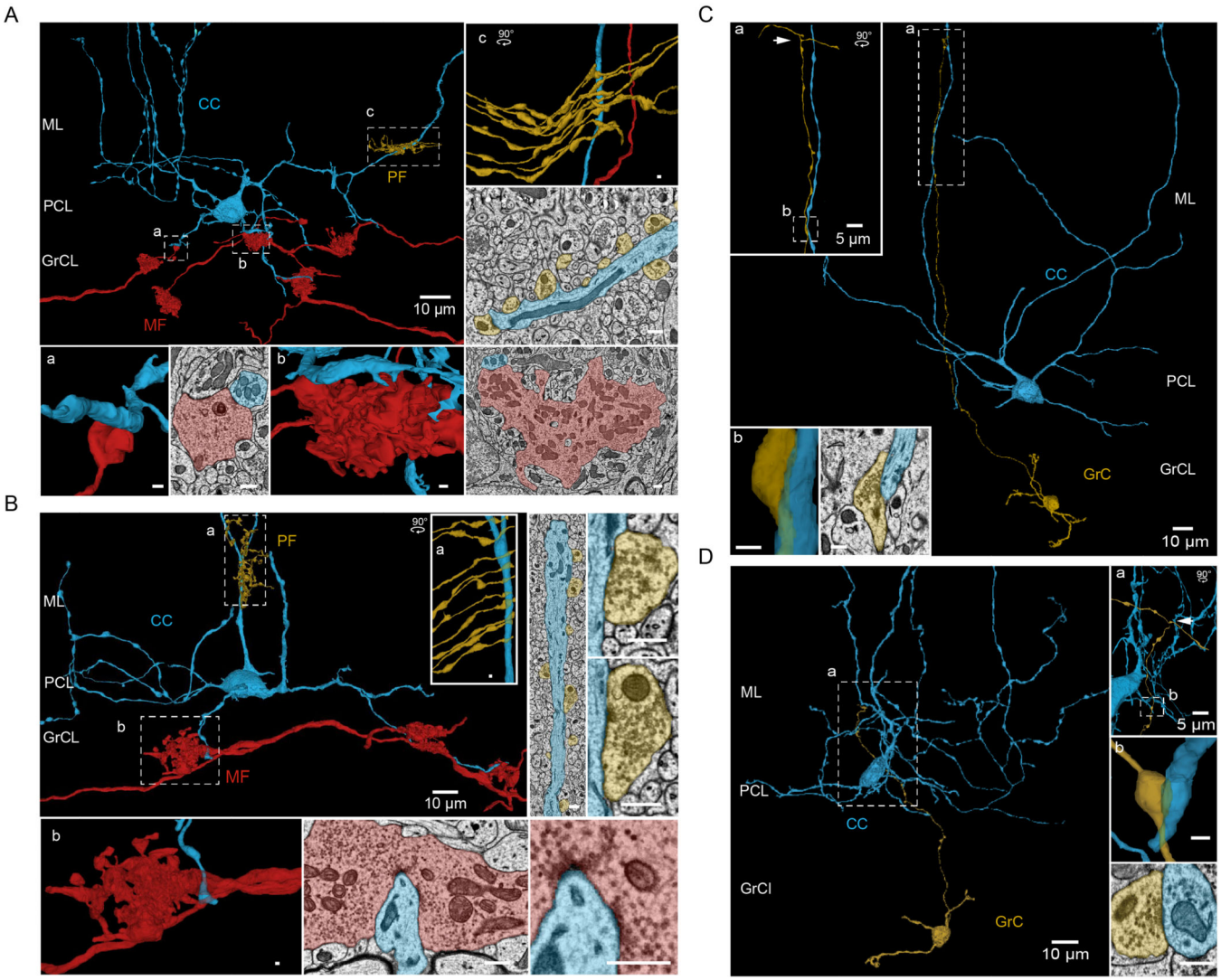

Extended Data Fig. 8. Examples of mossy fiber and granule cell excitatory inputs to CCs

A) EM reconstruction of a candelabrum cell (blue) and examples of connected mossy fibers (red) and granule cell parallel fibers (gold). Dashed boxes denote regions of insets shown to the right and on the bottom of the Fig. (a, b, c). a, example of extraglomerular MF synapse onto the basal dendrite of a CC. Left, reconstruction; right, single-plane EM image detailing the synapse. b, example of glomerular MF synapse onto the basal dendrite of a CC. Left, reconstruction; right, single-plane EM images. c, PF synapses into the apical dendrite of a CC. Left, reconstruction shown in in a horizontal orientation; right, single-plane EM images of PF-CC synapses.

B) Same as A for a different CC. a, example of parallel fiber synapses. Left, reconstruction in a horizontal orientation; right, single-plane EM image with synapse details. b, example of a glomerular mossy fiber synapse. Left, reconstruction; middle and right, single-plane EM images showing details of the synapse. Inset scalebars: 500 nm.

C and D) Examples of granule cell ascending branch (yellow) excitatory inputs to CCs (blue) for two different cells. Horizontal views of the ascending branch showing the location

of the synapse (dashed boxes) and the bifurcation into a parallel fiber (arrow). Dashed boxes denote regions also shown in expanded views along with corresponding EM sections. Inset scalebars: 500 nm.

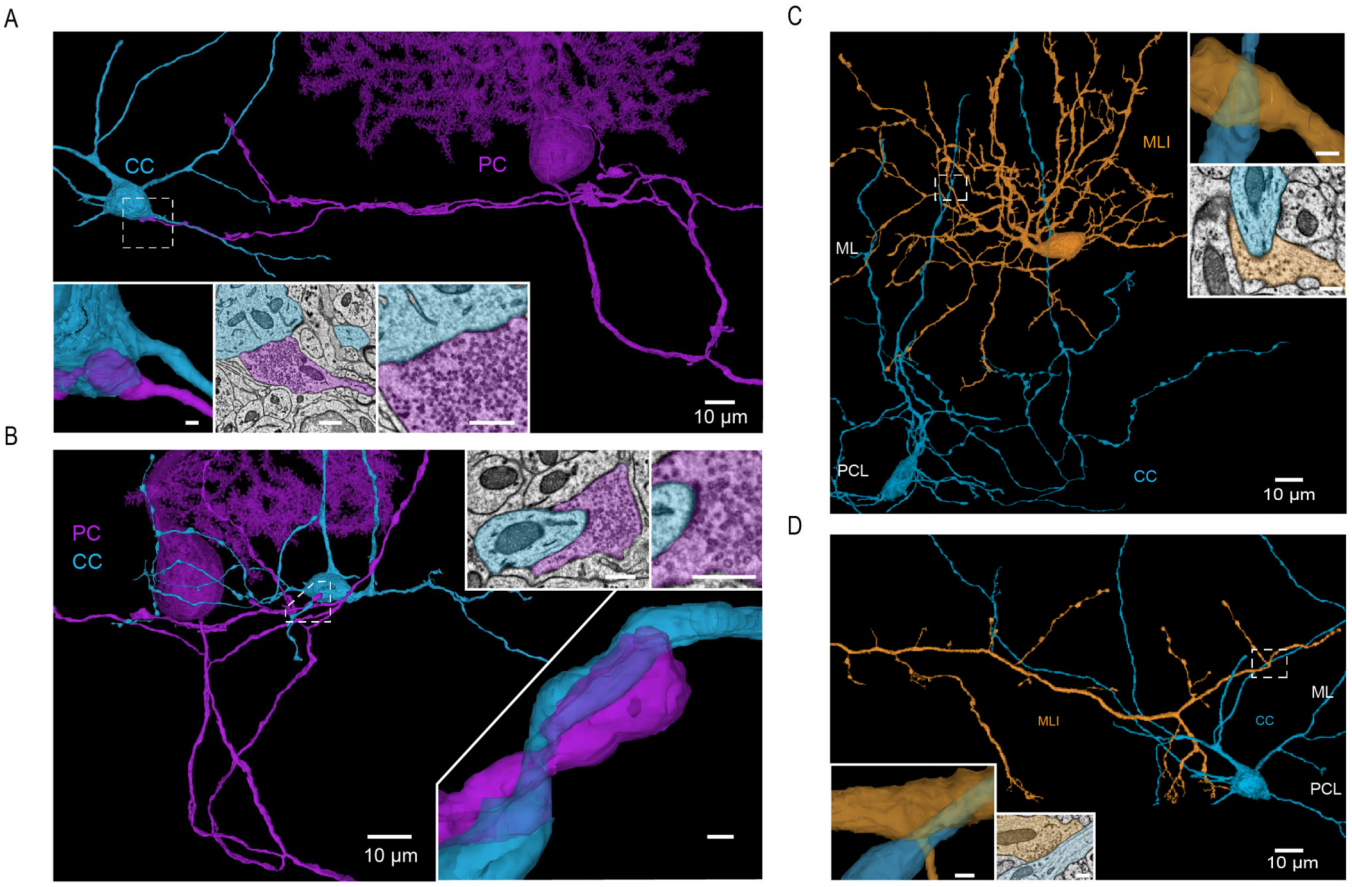

Extended Data Fig. 9. Additional examples of Purkinje cell (A,B. purple) and MLI (C,D. orange) synapses onto candelabrum cells (light blue)

A) Purkinje cell (purple) synapse onto a candelabrum cell.

B) Same as A for a different candelabrum cell.

C) An MLI with stellate cell morphology (orange) synapse onto a candelabrum cell.

D) An MLI with basket cell morphology (orange) synapse onto a candelabrum cell.

Dashed boxes denote regions shown in insets. Insets show an expanded view of the reconstruction along with single-plane EM sections showing the details of the synapse. Inset scalebars: 500 nm.

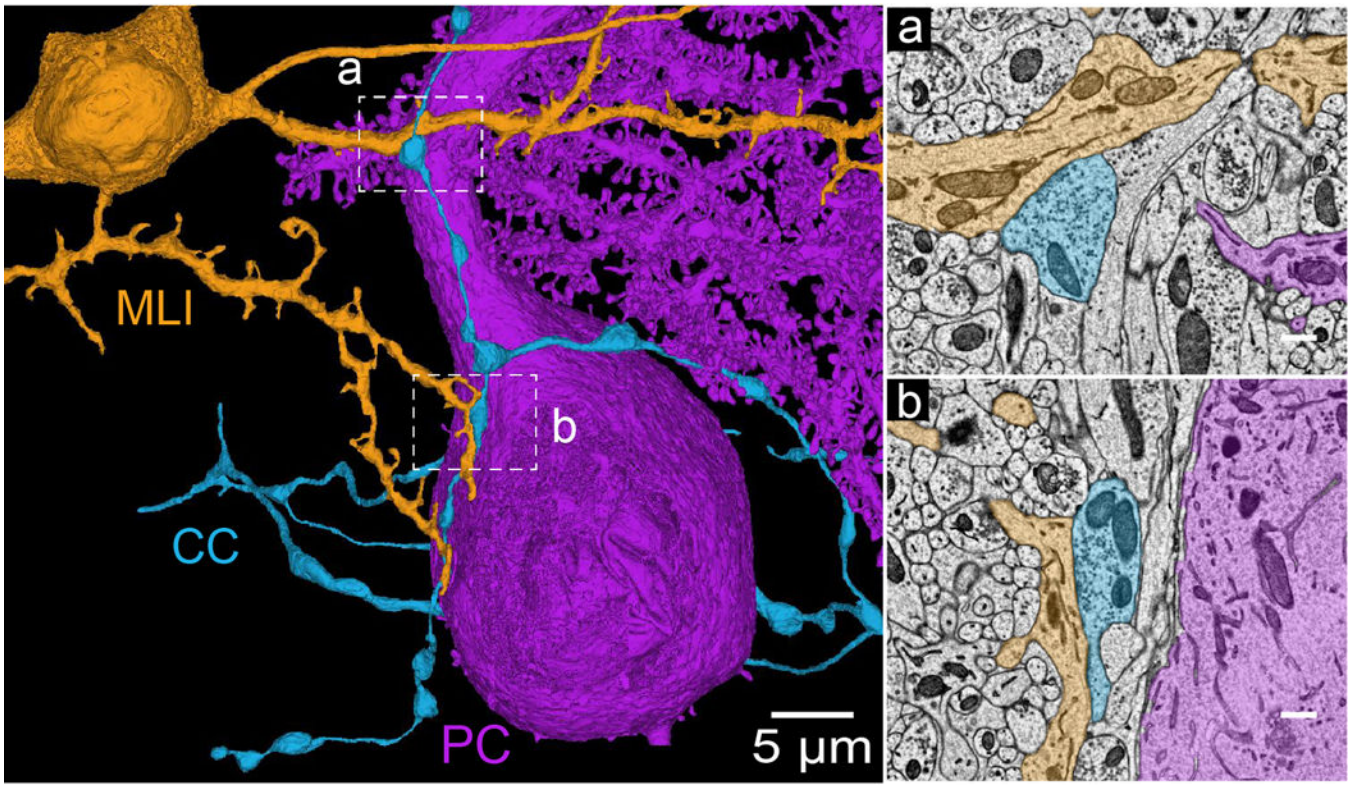

Extended Data Fig. 10. The importance of serial EM in identifying synaptic contacts

The same field of view from Extended Data Fig. 9B is shown, with a CC axon (light blue), a synaptically-connected MLI (orange) and a PC (purple). The axon of the CC ascends very close to the PC, but does not form any synapses onto the PC. Two synapses onto an MLI are shown in the dashed boxes (a,b), along with their respective single-plane EM sections. Inset scalebars: 500 nm. This figure illustrates the importance of EM in identifying synaptic contacts, and how reconstructed cells, and likely fluorescence images, have limitations.

Supplementary Material

Refer to Web version on PubMed Central for supplementary material.

ACKNOWLEDGMENTS

We thank members of the Regehr lab and Gord Fishell for comments on the manuscript. This work was supported by grants from the NIH, R01NS032405 and R35NS097284 to W.G.R, NIH/NIMH Brain Grant 1U19MH114821 to E.Z.M., the Stanley Center for Psychiatric Research and by the Vision Core and NINDS P30 Core Center (NS072030) to the Neurobiology Imaging Center at Harvard Medical School. The funders had no role in study design, data collection and analysis, decision to publish or preparation of the manuscript.

REFERENCES

1. Schmahmann JD The cerebellum and cognition. Neurosci Lett 688, 62–75 (2019). [PubMed: 29997061]
2. Sokolov AA, Miall RC & Ivry RB The Cerebellum: Adaptive Prediction for Movement and Cognition. Trends Cogn Sci 21, 313–332 (2017). [PubMed: 28385461]

3. Wang SS, Kloth AD & Badura A. The cerebellum, sensitive periods, and autism. Neuron 83, 518–532 (2014). [PubMed: 25102558]
4. Strick PL, Dum RP & Fiez JA Cerebellum and nonmotor function. Annu Rev Neurosci 32, 413–434 (2009). [PubMed: 19555291]
5. D'Angelo E, et al. The cerebellar Golgi cell and spatiotemporal organization of granular layer activity. Front Neural Circuits 7, 93 (2013). [PubMed: 23730271]
6. Duguid I, et al. Control of cerebellar granule cell output by sensory-evoked Golgi cell inhibition. Proc Natl Acad Sci U S A 112, 13099–13104 (2015). [PubMed: 26432880]
7. Mitchell SJ & Silver RA GABA spillover from single inhibitory axons suppresses low-frequency excitatory transmission at the cerebellar glomerulus. J Neurosci 20, 8651–8658 (2000). [PubMed: 11102470]
8. Kim J. & Augustine GJ Molecular Layer Interneurons: Key Elements of Cerebellar Network Computation and Behavior. Neuroscience (2020).
9. Jorntell H, Bengtsson F, Schonewille M. & De Zeeuw CI Cerebellar molecular layer interneurons - computational properties and roles in learning. Trends Neurosci 33, 524–532 (2010). [PubMed: 20869126]
10. Kozareva V, et al. A transcriptomic atlas of mouse cerebellar cortex comprehensively defines cell types. Nature 598, 214–219 (2021). [PubMed: 34616064]
11. Tasic B, et al. Shared and distinct transcriptomic cell types across neocortical areas. Nature 563, 72–78 (2018). [PubMed: 30382198]
12. Adkins RS, et al. A multimodal cell census and atlas of the mammalian primary motor cortex. bioRxiv, 2020.2010.2019.343129 (2020).
13. Yao Z, et al. An integrated transcriptomic and epigenomic atlas of mouse primary motor cortex cell types. bioRxiv, 2020.2002.2029.970558 (2020).
14. Bakken TE, et al. Evolution of cellular diversity in primary motor cortex of human, marmoset monkey, and mouse. bioRxiv, 2020.2003.2031.016972 (2020).
15. Laine J. & Axelrad H. The candelabrum cell: a new interneuron in the cerebellar cortex. J Comp Neurol 339, 159–173 (1994). [PubMed: 8300903]
16. Gouwens NW, et al. Integrated Morphoelectric and Transcriptomic Classification of Cortical GABAergic Cells. Cell 183, 935–953 e919 (2020). [PubMed: 33186530]
17. Dieudonne S. & Dumoulin A. Serotonin-driven long-range inhibitory connections in the cerebellar cortex. J Neurosci 20, 1837–1848 (2000). [PubMed: 10684885]
18. Palay SL & Chan-Palay V. Cerebellar Cortex (Springer, Berlin, Heidelberg, 1974).
19. Sahin M. & Hockfield S. Molecular identification of the Lugaro cell in the cat cerebellar cortex. J Comp Neurol 301, 575–584 (1990). [PubMed: 2273099]
20. Dieudonne S. Serotonergic neuromodulation in the cerebellar cortex: cellular, synaptic, and molecular basis. Neuroscientist 7, 207–219 (2001). [PubMed: 11499400]
21. Simat M, Parpan F. & Fritschy JM Heterogeneity of glycinergic and gabaergic interneurons in the granule cell layer of mouse cerebellum. J Comp Neurol 500, 71–83 (2007). [PubMed: 17099896]
22. Laine J. & Axelrad H. Morphology of the Golgi-impregnated Lugaro cell in the rat cerebellar cortex: a reappraisal with a description of its axon. J Comp Neurol 375, 618–640 (1996). [PubMed: 8930789]
23. Geurts FJ, Timmermans J, Shigemoto R. & De Schutter E. Morphological and neurochemical differentiation of large granular layer interneurons in the adult rat cerebellum. Neuroscience 104, 499–512 (2001). [PubMed: 11377850]
24. Geurts FJ, De Schutter E. & Timmermans JP Localization of 5-HT2A, 5-HT3, 5-HT5A and 5-HT7 receptor-like immunoreactivity in the rat cerebellum. J Chem Neuroanat 24, 65–74 (2002). [PubMed: 12084412]
25. Laine J. & Axelrad H. Extending the cerebellar Lugaro cell class. Neuroscience 115, 363–374 (2002). [PubMed: 12421603]
26. Hirono M, et al. Cerebellar globular cells receive monoaminergic excitation and monosynaptic inhibition from Purkinje cells. PLoS One 7, e29663 (2012). [PubMed: 22235322]

27. Chabrol FP, Arenz A, Wiechert MT, Margrie TW & DiGregorio DA Synaptic diversity enables temporal coding of coincident multisensory inputs in single neurons. Nat Neurosci 18, 718–727 (2015). [PubMed: 25821914]
28. Kanichay RT & Silver RA Synaptic and cellular properties of the feedforward inhibitory circuit within the input layer of the cerebellar cortex. J Neurosci 28, 8955–8967 (2008). [PubMed: 18768689]
29. Nietz AK, Vaden JH, Coddington LT, Overstreet-Wadiche L. & Wadiche JI Non-synaptic signaling from cerebellar climbing fibers modulates Golgi cell activity. Elife 6 (2017).
30. Szapiro G. & Barbour B. Multiple climbing fibers signal to molecular layer interneurons exclusively via glutamate spillover. Nat Neurosci 10, 735–742 (2007). [PubMed: 17515900]
31. Coddington LT, Rudolph S, Vande Lune P, Overstreet-Wadiche L. & Wadiche JI Spillover-mediated feedforward inhibition functionally segregates interneuron activity. Neuron 78, 1050–1062 (2013). [PubMed: 23707614]
32. Mathews PJ, Lee KH, Peng Z, Houser CR & Otis TS Effects of climbing fiber driven inhibition on Purkinje neuron spiking. J Neurosci 32, 17988–17997 (2012). [PubMed: 23238715]
33. Witter L, Rudolph S, Pressler RT, Lahlaf SI & Regehr WG Purkinje Cell Collaterals Enable Output Signals from the Cerebellar Cortex to Feed Back to Purkinje Cells and Interneurons. Neuron 91, 312–319 (2016). [PubMed: 27346533]
34. Mann-Metzer P. & Yarom Y. Electrotonic coupling interacts with intrinsic properties to generate synchronized activity in cerebellar networks of inhibitory interneurons. J Neurosci 19, 3298–3306 (1999). [PubMed: 10212289]
35. Dugue GP, et al. Electrical coupling mediates tunable low-frequency oscillations and resonance in the cerebellar Golgi cell network. Neuron 61, 126–139 (2009). [PubMed: 19146818]
36. Saunders A, et al. Molecular Diversity and Specializations among the Cells of the Adult Mouse Brain. Cell 174, 1015–1030 e1016 (2018). [PubMed: 30096299]
37. Schilling K, Oberdick J, Rossi F. & Baader SL Besides Purkinje cells and granule neurons: an appraisal of the cell biology of the interneurons of the cerebellar cortex. Histochem Cell Biol 130, 601–615 (2008). [PubMed: 18677503]
38. Qian X, et al. Probabilistic cell typing enables fine mapping of closely related cell types in situ. Nat Methods 17, 101–106 (2020). [PubMed: 31740815]
39. Pelkey KA, et al. Hippocampal GABAergic Inhibitory Interneurons. Physiol Rev 97, 1619–1747 (2017). [PubMed: 28954853]
40. Friesen WO & Stent GS Generation of a locomotory rhythm by a neural network with reccurrent cyclic inhibition. Biol Cybern 28, 27–40 (1977). [PubMed: 597508]
41. Horikawa Y. Exponential transient propagating oscillations in a ring of spiking neurons with unidirectional slow inhibitory synaptic coupling. J Theor Biol 289, 151–159 (2011). [PubMed: 21893072]
42. Vervaeke K, et al. Rapid desynchronization of an electrically coupled interneuron network with sparse excitatory synaptic input. Neuron 67, 435–451 (2010). [PubMed: 20696381]
43. Miyazaki T, Yamasaki M, Tanaka KF & Watanabe M. Compartmentalized Input-Output Organization of Lugaro Cells in the Cerebellar Cortex. Neuroscience (2020).
44. Rowan MJM, et al. Graded Control of Climbing-Fiber-Mediated Plasticity and Learning by Inhibition in the Cerebellum. Neuron 99, 999–1015 e1016 (2018). [PubMed: 30122378]
45. Verheugen JA, Fricker D. & Miles R. Noninvasive measurements of the membrane potential and GABAergic action in hippocampal interneurons. J Neurosci 19, 2546–2555 (1999). [PubMed: 10087068]
46. Welch JD, et al. Single-Cell Multi-omic Integration Compares and Contrasts Features of Brain Cell Identity. Cell 177, 1873–1887 e1817 (2019). [PubMed: 31178122]
47. Qiu X, et al. Reversed graph embedding resolves complex single-cell trajectories. Nat Methods 14, 979–982 (2017). [PubMed: 28825705]
48. Gerfen CR, Paletzki R. & Heintz N. GENSAT BAC cre-recombinase driver lines to study the functional organization of cerebral cortical and basal ganglia circuits. Neuron 80, 1368–1383 (2013). [PubMed: 24360541]

49. Overstreet LS, et al. A transgenic marker for newly born granule cells in dentate gyrus. J Neurosci 24, 3251–3259 (2004). [PubMed: 15056704]

50. Cheadle L, et al. Sensory Experience Engages Microglia to Shape Neural Connectivity through a Non-Phagocytic Mechanism. Neuron 108, 451–468 e459 (2020). [PubMed: 32931754]

51. Phelps JS, et al. Reconstruction of motor control circuits in adult Drosophila using automated transmission electron microscopy. Cell 184, 759–774 e718 (2021). [PubMed: 33400916]

52. Funke J, et al. Large Scale Image Segmentation with Structured Loss Based Deep Learning for Connectome Reconstruction. IEEE Trans Pattern Anal Mach Intell 41, 1669–1680 (2019). [PubMed: 29993708]

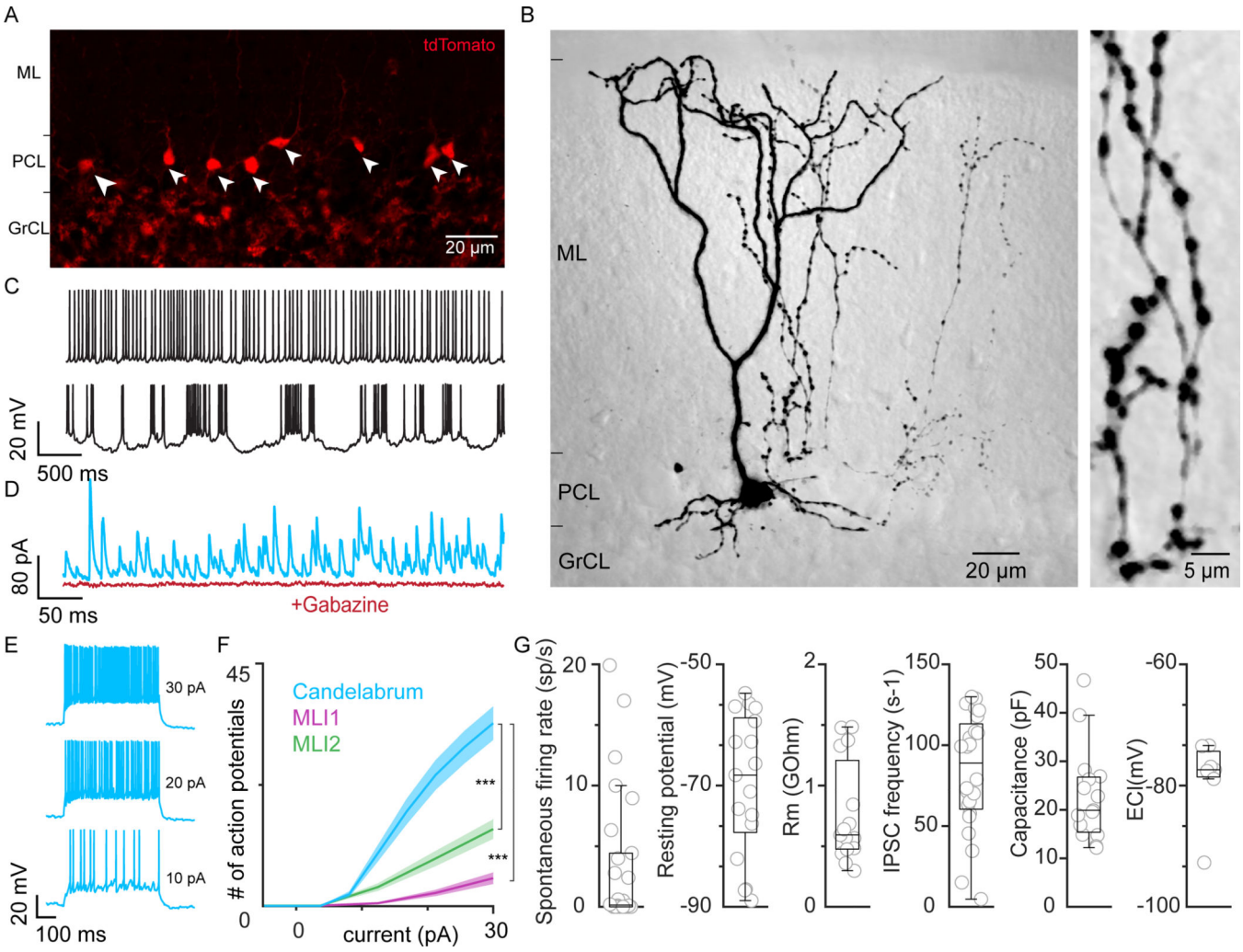

Fig. 1. Determining the morphological and electrophysiological properties of candelabrum cells using Oxtr-Cre × Ai14 (tdTomato) mice.

A. Sagittal cerebellar cortex section of an Oxtr-Cre × Ai14 mouse shows small cells in the PCL (red, white arrows) and MFs labeled with tdTomato (red) in the granule cell layer.

B. 2-photon image of an Alexa-594 labelled candelabrum cell. Image to the right is an expanded image of the axon.

C. Spontaneous activity in a regular firing (top) and burst firing (bottom) candelabrum cell.

D. Spontaneous IPSCs recorded in a candelabrum cell in the absence of synaptic blockers (light blue) and after wash-in of the $GABA_AR$ antagonist gabazine (10 µM, red).

E. Examples of action potential firing evoked by current injection of 10, 20 and 30 pA.

F. Average input-output curve of candelabrum cells, compared to the input-output curve of two types of molecular layer interneurons, MLI1 and MLI2 (data from Kozareva et al. 2021). Shaded area represents ± s.e.m. p=2.1e-18 (for slope MLI1/CC), p= 7.5e-10 (for slope MLI2/CC), the data was fit with a generalized mixed effects model and the coefficients were tested with a two sided unpaired t-test without multiple comparison correction. (MLI1: n=22 cells; MLI2: n=20 cells; CC: n=18 cells).

G. Summary of basic electrophysiological properties of candelabrum cells. (n=26,17,15, 24,15, 7 cells). In box plots, box outlines and center line indicate median and interquartile range, and the whiskers indicate data points up to 1.5x interquartile range.

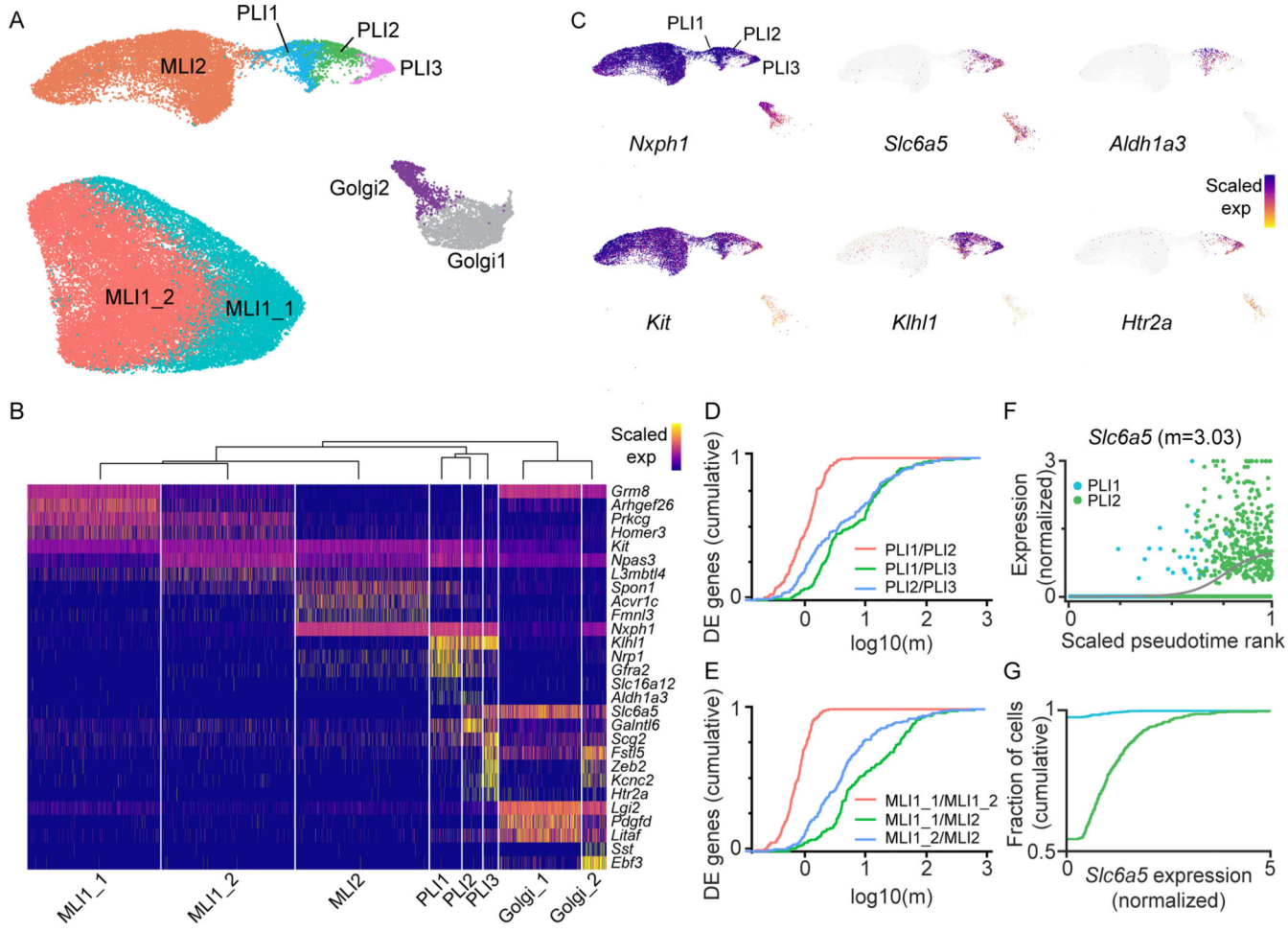

Fig. 2. Molecular characterization of cerebellar inhibitory interneurons with snRNAseq.

A. UMAP plot of snRNAseq of cerebellar inhibitory interneurons. MLI1 and ML2 are types of molecular layer interneurons, and MLI1 can be further subdivided into MLI1_1 and MLI1_2. Golgi1 and Golgi2 are types of Golgi cells. Purkinje cell layer interneurons are divided into PLI1, PLI2 and PLI3.

B. Scaled RNA expression of key genes in cerebellar inhibitory interneurons.

C. UMAP plots of *Nxph1*, *Slc6a5*, *Aldh1a3*, *Kit*, *Klhl1* and *Htr2a* expression in MLI2, PLIs and Golgi2 cells. Colormap maximum values were adjusted for each gene (*Nxph1*: 5.5, *Slc6a5/Htr2a*: 2.5, *Aldh1a3*: 2, *Kit/Klh1*: 3.5)

D. Cumulative distributions of *m* values from logistic curve fits along the pseudotime axis for top differentially expressed (DE) genes among aggregated combinations of PLIs.

E. Same as D but for aggregated combinations of molecular layer interneuron subtypes.

F. *Slc6a5* expression in single PLI1s and PLI2s as a function of pseudotime.

G. Fraction of PLI1s and PLI2s expressing Slc6a5 in snRNAseq experiments.

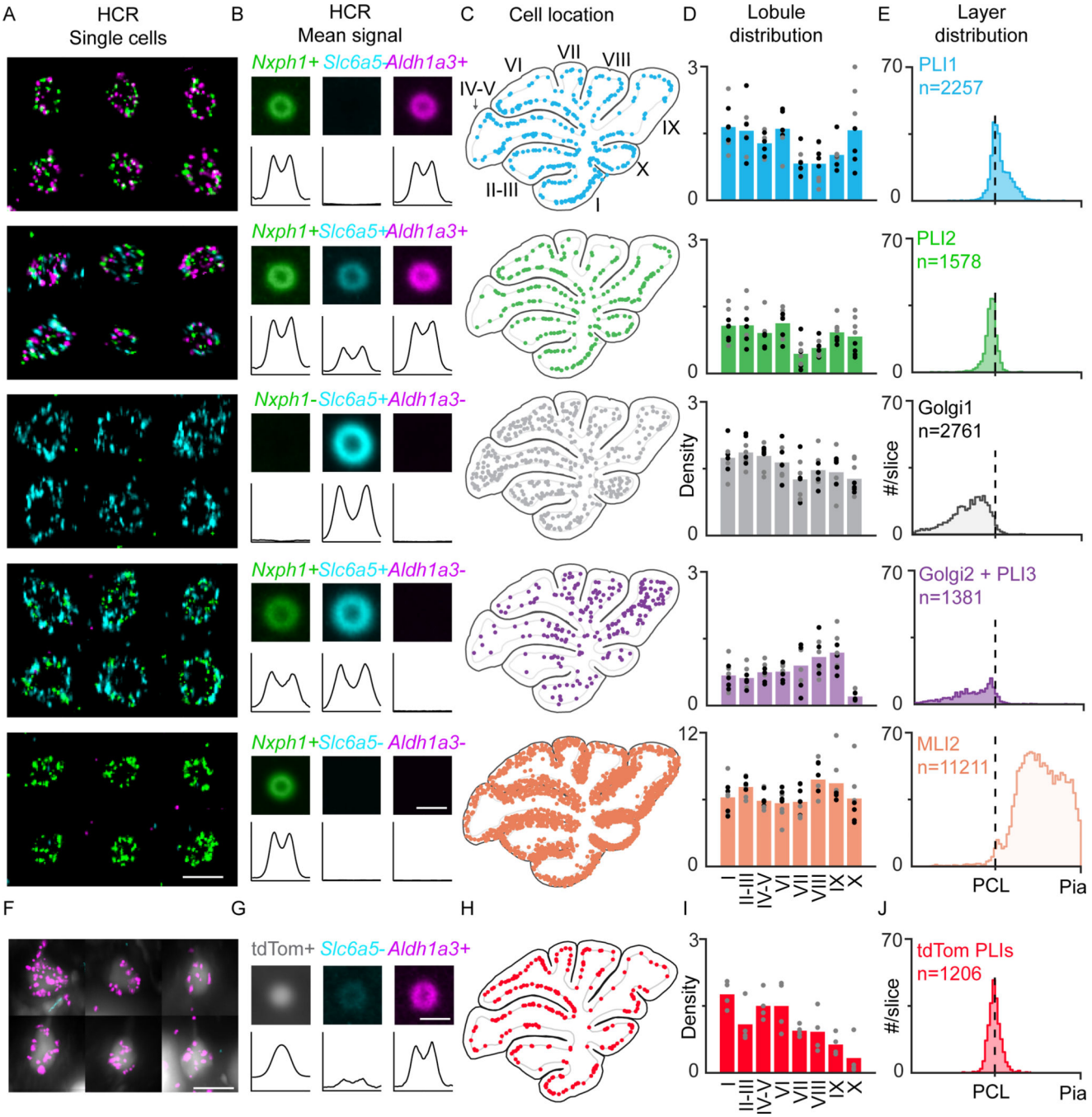

Fig. 3. Identification of different types of interneurons in the cerebellar cortex with fluorescent in situ hybridization.

A. Example labeling of single cells for five different classes of cells with probes for *Nxph1*, *Aldh1a3* and *Slc6a5* RNA (top to bottom):

Candelabrum cell (PLI1): *Nxph1*+, *Slc6a5*−, *Aldh1a3*+

Globular cell (PLI2): *Nxph1*+, *Slc6a5*+, *Aldh1a3*+

Golgi1: *Nxph1*−, *Slc6a5*+, *Aldh1a3*−

Golgi2 + Lugaro cells (PLI3): *Nxph1+, Slc6a5*+, *Aldh1a3*−

MLI2: *Nxph1*+, *Slc6a5*−, *Aldh1a3*−. Scalebar=10μm.

B. Mean fluorescence signals of three probes in the five interneuron populations. Lower plots show intensity profiles for each channel. Scalebar = 10μm.
C. Locations of cells in a single slice for five interneuron populations.
D. Average normalized densities of different types of interneurons in different lobules. Each point is from a different slice, male (black) female (gray). n=8 slices. Density is the number of cells per 100 μm of PCL in each slice. Bar height denotes the mean value.
E. Histograms of the locations of each interneuron type relative to the center of the PCL (average of 8 slices), and the top of the molecular layer (pia).
F-J Same as A-E for tdTomato+ PLIs in Oxtr-Cre × Ai14 mice. Four slices are summarized in I and J. Background tdTomato labelling was prominent in lobule X and likely resulted in an underestimate of tdTomato-labelled PLIs in lobule X. This may account for the lower number of cells in lobule X in I compared to the number of PLI1s in D. Color scales for A,F denote pixel values: 200–750 for Nxph1 (green), 200–1500 for Slc6a5 and Aldh1a3 (cyan, magenta), and 0–15000 for tdTomato (gray). For average images and profiles in B,G, the color scales denote pixel values: 0–185 for Nxph1, 0–370 for Slc6a5 and Aldh1a3, and 0–5400 for tdTomato (gray).

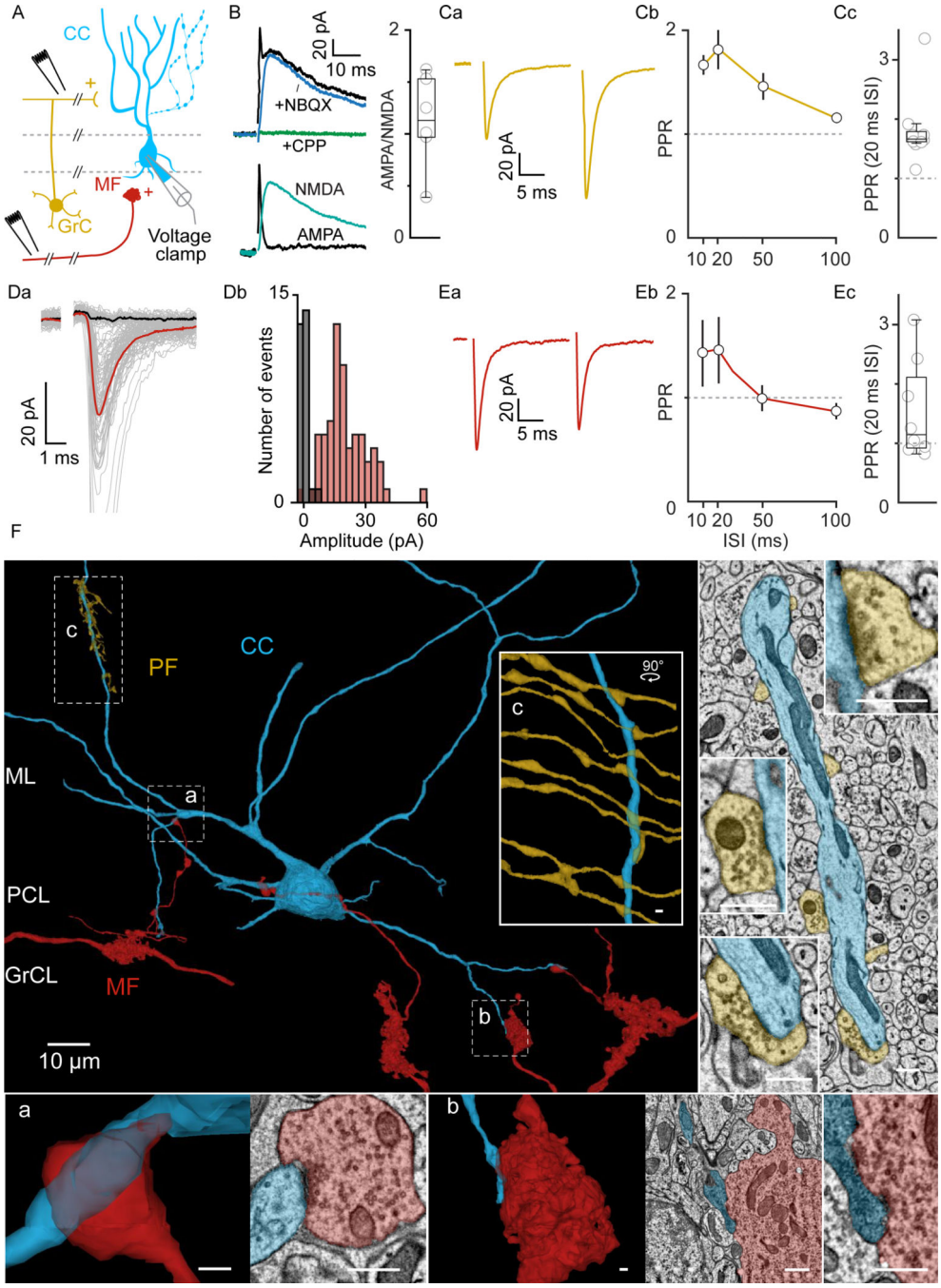

Fig. 4. Synaptic excitation of candelabrum cells.

A) Schematic of the experimental configuration. EPSCs were recorded from candelabrum cells (CC, blue) in whole-cell voltage clamp during electrical stimulation of granule cell (GrC) parallel fibers (PFs) in the molecular layer, or MFs (red) in the white matter.

B) (*top*) Example of synaptic currents evoked by stimulation of GrC axons for a CC held at +40 mV, in control conditions, in the presence of NBQX and in the presence of CPP. (*bottom)* The AMPA component (control – NBQX) and the NMDA component (NBQX-

[NBQX+CPP]) are shown in isolation. (right) The ratios of peak AMPA/NMDA are shown n=6 cells (right).

Ca) Example of facilitating GrC-mediated synaptic currents evoked by paired stimulation with an ISI of ~ 20 ms. The stimulus artifact was subtracted for clarity.

Cb) Summary data of paired-pulse ratio of GrC-mediated currents evoked at varying ISIs (mean ± s.e.m). n=9 cells.

Cc) Summary of paired-pulse ratio of GrC-mediated currents for 20ms ISI. Dashed line indicates PPR=1. n=9 cells.

Da) Example of MF-mediated synaptic currents evoked by threshold stimulation. Individual trials (grey), average successes (red) and average failure (black) are shown. The stimulus artifact was blanked for clarity.

Db, left) Histogram of success and failure trials.

Ea) Example of non-facilitating MF-EPSC evoked by paired stimulation with an ISI of 20 ms. The stimulus artifact was blanked for clarity.

Eb) Summary of paired-pulse ratio for MF-EPSCs (mean ± s.e.m). n=8 cells.

Ec) Summary of paired-pulse ratio of MF-mediated currents for 20ms ISI. Dashed line indicates PPR=1. n=8 cells. In all box plots, box outlines and center line indicate median and interquartile range, and the whiskers indicate data points up to 1.5x interquartile range.

F) A CC (blue), and synaptically connected PFs (gold) and MFs (red) reconstructed from serial EM images are shown. Dashed boxes denote regions of insets shown to the right and on the bottom of the Fig. (a, b, c). a, example of extraglomerular MF synapse onto the basal dendrite of a CC. Left, reconstruction; right, single-plane EM image. b, example of glomerular MF synapse onto the basal dendrite of a CC. Left, reconstruction; right, single-plane EM image. c, PF synapses into the apical dendrite of a CC. Right, single-plane EM images of PF-CC synapses. Inset scalebars: 500 nm.

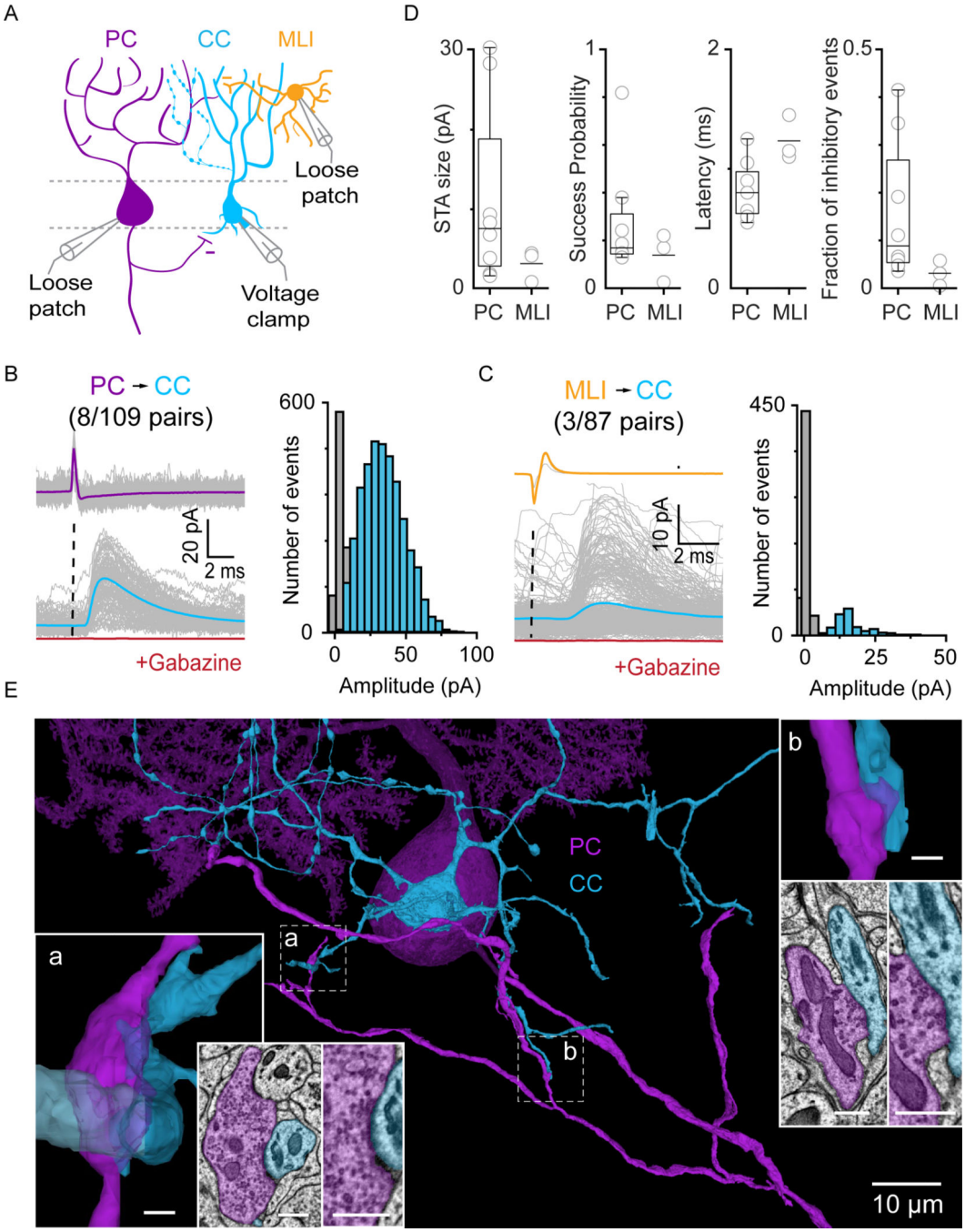

Fig. 5. Synaptic Inhibition of candelabrum cells.

A) Schematic of the experimental configuration. IPSCs were recorded from a candelabrum cell (CC, blue) in whole-cell voltage clamp and spontaneous action potentials were recorded from a synaptically connected PC (purple) or MLI (orange) in loose-patch configuration.

B) Left, aligned PC spikes (grey: individual spikes, purple: average), and CC recordings (grey: individual traces, blue: average. Gabazine (10 µM) wash-in eliminated IPSCs in the CC (red trace). Dashed line represents the peak of the action potential.

B, right) Amplitude histogram of IPSCs after a PC spike (blue: successes, grey: failures).

C, left) Aligned MLI spikes (grey: individual spikes, orange: average), and CC recordings (grey: individual traces, blue: average. Gabazine wash-in eliminated IPSCs in the CC (red trace). Dashed line represents the peak of the action potential.
C, right) Amplitude histogram of IPSCs after a MLI spike (blue: successes, grey: failures).
D) Summary of the properties of PC to CC synapses (n=8/109 pairs), and MLI to CC synapses (n=3/87 pairs). STA: spike triggered average. In box plots, box outlines and center line indicate median and interquartile range, and the whiskers indicate data points up to 1.5x interquartile range.
E) EM reconstruction shows a PC (purple) that is synaptically connected to a CC (blue). Dashed boxes denote regions also shown in expanded views along with corresponding EM sections. Scalebars in insets are 500 nm.

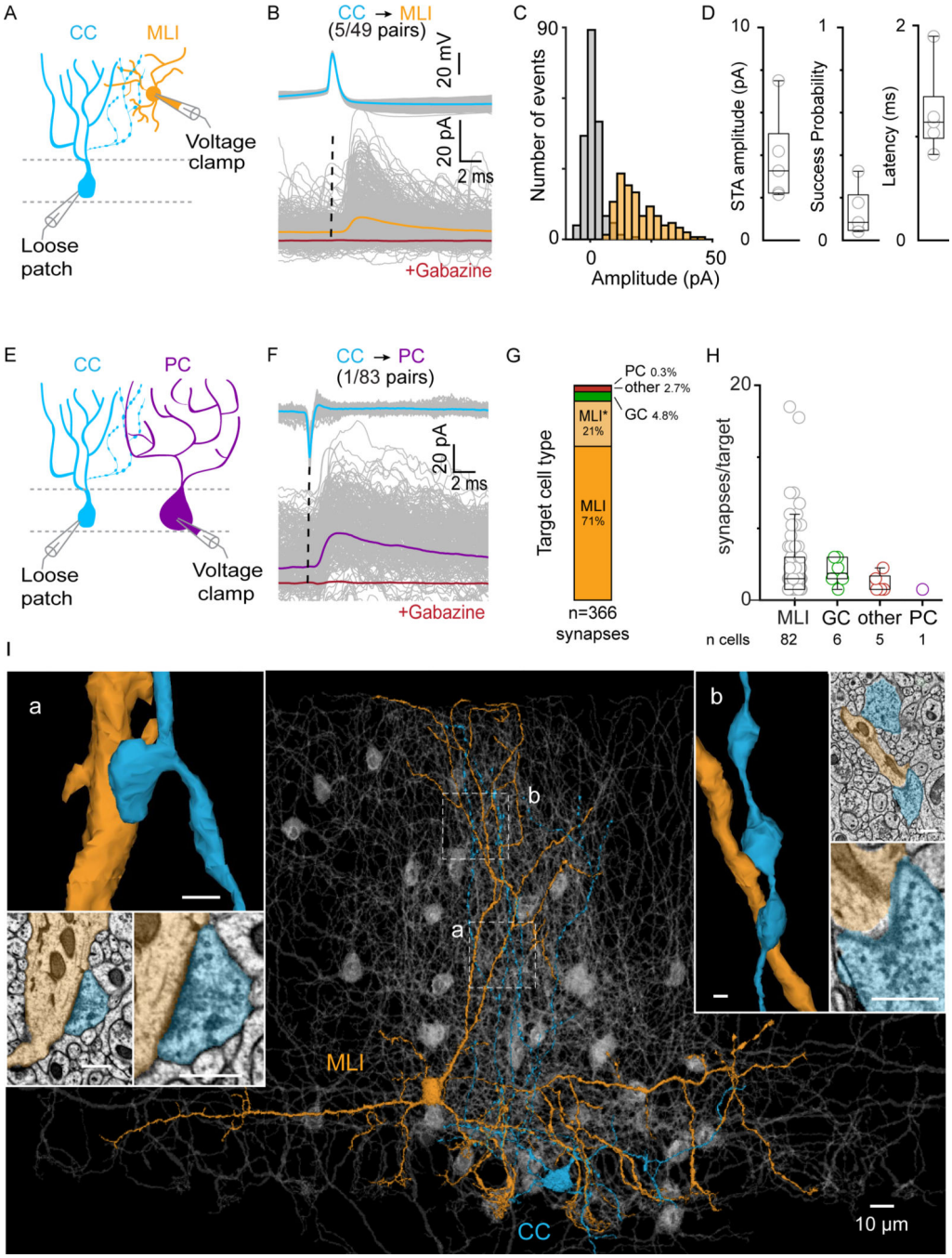

Fig. 6. Candelabrum cell mediated inhibition of target neurons

A. Recording configuration is shown in which spontaneous action potentials were recorded from CCs in loose patch or current clamp, and MLIs were simultaneously recorded in voltage clamp.

B. Aligned CC action potentials (top, grey: individual traces, blue: average) and MLI traces (bottom, grey: individual traces, orange: average, red: average in the presence of gabazine). Dashed line represents the peak of the action potential.

C. Histogram of IPSC amplitudes in B (orange: successes, grey: failures).

D. Summary of properties of CC to MLI connections. n=5/50 pairs STA: spike triggered average.

E. Recording configuration is shown. Spontaneous action potentials were recorded from CCs in loose patch or current clamp, and PCs were simultaneously recorded in voltage clamp.

F. Aligned CC action potentials (top, grey: individual traces, blue: average trace) and corresponding IPSCs in PCs (bottom, grey: individual traces, purple: average, red: average in the presence of gabazine).

G. The targets of 366 CC synapses were identified. MLI* denotes putative molecular layer interneurons cells that could only be partially reconstructed. Other denotes Golgi cells and PLIs that could only be partially reconstructed. n=3 candelabrum cells.

H. Summary of the number of CC output synapses per target cell, from EM reconstructions. In all box plots, box outlines and center line indicate median and interquartile range, and the whiskers indicate data points up to 1.5x interquartile range. n=3 candelabrum cells, 366 synapses.

I. EM reconstruction of a CC (blue) and its postsynaptic target cells (grey). One target basket cell is highlighted (orange). Dashed boxes denote regions of insets showing example synapses onto this cell. a, b CC axon boutons contacting a basket cell dendrite with corresponding single sections. Inset scalebars: 500 nm.

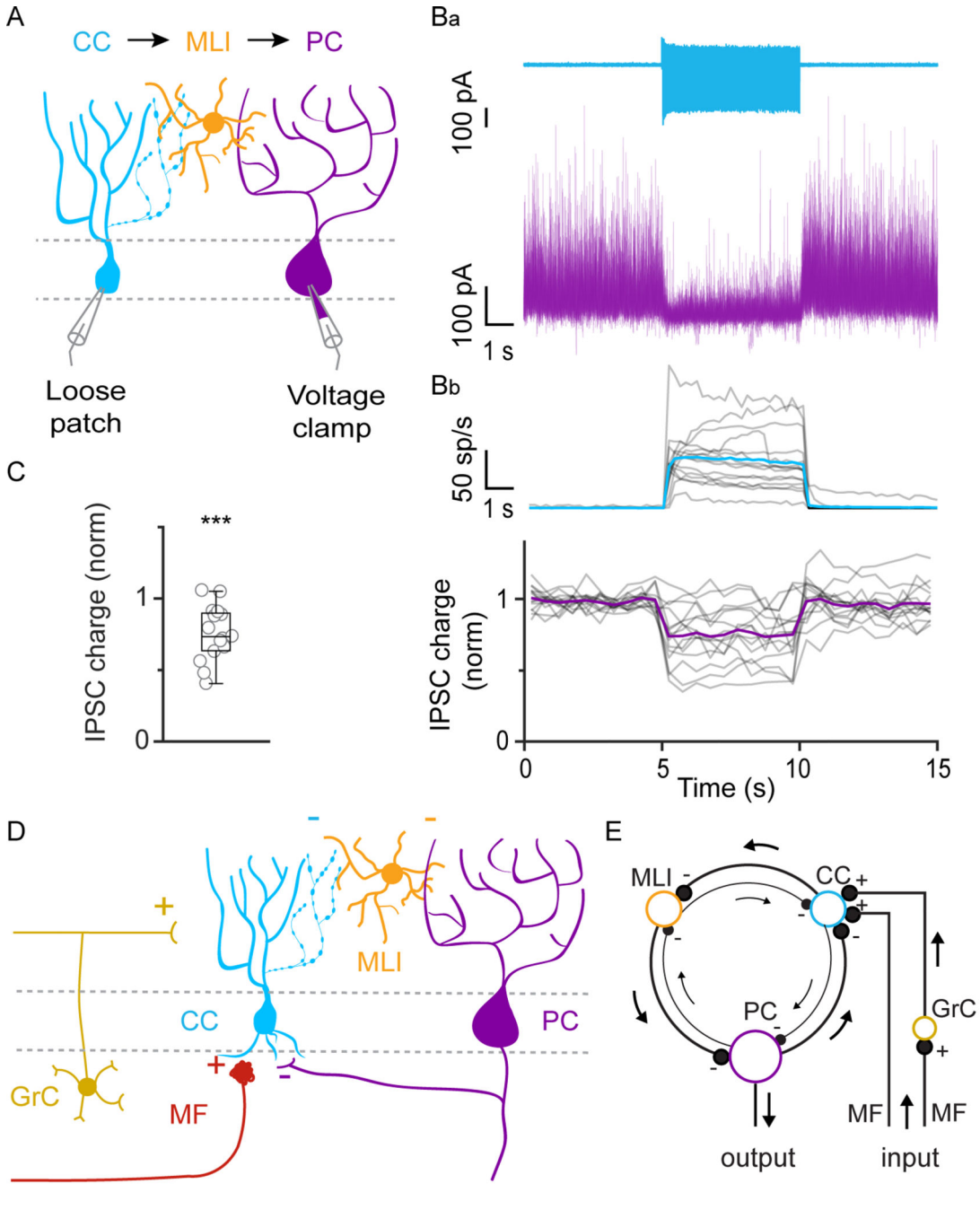

Fig. 7. Candelabrum cells disinhibit Purkinje cells.

A. Schematic showing experimental configuration of paired recordings in which a CC was stimulated while recording spontaneous IPSCs in PCs.

Ba. Elevated evoked CC activity (light blue) decreases spontaneous inhibition of PCs (purple). Capacitative currents have been removed for clarity.

Bb. Summary of the time course of CC firing and total IPSC charge in PCs. Grey traces show the mean of individual cells (≥5 trials), and colored traces show the mean of all cells. n=15 pairs.

C. Summary the effect of CC excitation on PC inhibition. p= 3.1e-04, two-sided Wilcoxon signed rank test, n=15 pairs. In box plot, box outlines and center line indicate median and interquartile range, and the whiskers indicate data points up to 1.5x interquartile range.
D. Schematic of the circuitry of the CC within the cerebellar cortex.
E. Schematic showing the loop of inhibitory neurons comprised of PCs, CCs, and MLIs and the regulation of CC firing by PCs, MFs and granule cells.